International Journal of Machine Tools & Manufacture 209 (2025) 104296

Contents lists available at ScienceDirect

International Journal of Machine Tools and Manufacture

journal homepage: www.elsevier.com/locate/ijmactool

Research Article

A novel computational approach using receptance coupling substructure analysis for prediction of tool tip dynamics in industrial machining applications

Jesus David Chaux *, Patxi X. Aristimuño Osoro, Pedro J. Arrazola

Faculty of Engineering, Mondragon Unibertsitatea, Mondragon, 20500, Spain

Nomenclature

Symbol	Description
ω	Frequency [rad/s]
θ	Angular coordinate [rad]
ξ	Axial coordinate [m]
f	Force [N]
m	Moment [N·m]
s	Measurement spacing position [m, mm]
K_{HT}	Contact stiffness matrix between tool holder and cutting tool
H_{ij}	Displacement-to-force receptance [m/N]; i is the measurement point, and j is the excitation point
L_{ij}	Displacement-to-moment receptance [m/(N·m)]; see H_{ij} for subscript details
N_{ij}	Rotation-to-force receptance [rad/N]; see H_{ij} for subscript details
P_{ij}	Rotation-to-moment receptance [rad/(N·m)]; see H_{ij} for subscript details
$[G_{ij}]_{nm}$	Receptance matrix at measurement point i and excitation point j. n indicates the assembly (H1: MSF-H1, H2: MSF-H2, T1: MSF-H1-T1, T2: MSF-H2-T2). m indicates the result source (Exp: experimental, RCSA: receptance coupling substructure analysis)
$[R]_n$	Receptance matrix of substructure n, which can be H1 for holder 1, H2 for holder 2, T1 for tool 1, and T2 for tool 2
D	Outer diameter [mm]
D_i	Inner diameter [mm]
E	Young's modulus [N/m^2]
ρ	Density [kg/m^3]
η	Solid damping factor
ν	Poisson ratio
L	Length [mm]
a_e	Radial depth of cut [mm]
a_p	Axial depth of cut [mm]
n	Spindle speed [rpm]
k_s	Specific cutting force [MPa]
z	Number of teeth
x, θ	Subscripts indicating direction of motion (translation x or rotation θ)
f, m	Subscripts indicating type of loading (force f or moment m)
ϕ_r	Mode shape vector for mode r
$\phi_r^{(n)}$	n-th derivative of the mode shape function
λ_r	Eigenvalue parameter for mode r
M_r	Measurement perturbation bound for mode shape r
σ_r	Standard deviation of measurements for mode shape r
s_{min}	Optimal measurement spacing position [mm]
$\bar{s}$	Normalised measurement spacing position (s/L)
$\bar{x}$	Normalised position coordinate (x/L)
α_r	Dimensionless frequency number for trigonometric terms in the r-th vibration mode
β_r	Dimensionless frequency number for hyperbolic terms in the r-th vibration mode
A_r	Mass normalisation constant for the r-th vibration mode
C_i	Coefficients for finite difference approximations or coefficients determined by boundary conditions in the Timoshenko beam equation
T	Truncation coefficient in finite difference approximations
ε	Small tolerance for vertex merging in STL slicing
A	Area [mm^2]
I_x, I_y, I_{xy}	Moments of inertia about the x, y axes, and product moment of inertia [mm^4]
P	Perimeter [mm]
κ	Curvature [mm^{-1}]
HR	Height ratio, normalised vertical position of slice
D_c	Normalised distance from centroid to global centre
z_{slice}	Vertical position of a slice [mm]
$K(x_i, x)$	Kernel function for Support Vector Machine
f_z	Feed per tooth [mm/tooth]
$a_{p,lim,power}$	Axial depth of cut limited by spindle power [mm]
P_{lim}	Power limit [kW]
K_{tc}, K_r	Cutting force coefficients [MPa]

1. Introduction

Reducing cycle times in new machining projects is crucial for manufacturers to maximise return on investment. In such cases, the aim is to increase the material removal rates by selecting the most suitable chatter-free cutting conditions, as determined by stability lobe diagrams (SLDs). However, obtaining reliable SLDs in the early stages of production remains a challenge at an industrial level. This is because it

* Corresponding author.
E-mail address: jdchaux@mondragon.edu (J.D. Chaux).

https://doi.org/10.1016/j.ijmachtools.2025.104296
Received 16 January 2025; Received in revised form 17 May 2025; Accepted 21 May 2025
Available online 23 May 2025

requires accurate prediction of tool tip dynamics, which traditionally demands both specialised expertise and extensive time investment to characterise numerous holder-tool combinations.

Receptance coupling substructure analysis (RCSA) has become a standard approach for predicting tool tip dynamics [1], reducing the need for experimental measurements. This approach analyses the dynamics of each substructure separately and then couples them to calculate the overall dynamics of the system [2]. The significant benefit of RCSA is its analytical efficiency and ability to seamlessly integrate measured and modelled data in the frequency domain. Components with relatively simple geometries can be modelled using classical beam theories, whereas more complex components, such as direct-drive milling spindles with proprietary design, can be measured (e.g., using standard tap-testing) and archived in databases for future use [1].

The modelling of complex cutting tool geometries has significantly progressed since the inception of RCSA by Schmitz and Donalson [3], who relied on a simplified Euler-Bernoulli beam theory for dynamic prediction. This foundational work was later expanded by Ertürk et al. [4], who utilised Timoshenko beam theory to account for shear deformation and rotational inertia effects, thereby improving the accuracy, particularly for non-slender tools. However, their approach remained constrained to simple geometries, limiting its applicability to tools with intricate or variable cross-sections.

Kivanc and Budak [5] advanced the representation of fluted tool geometries through an arc approximation method, which addressed some geometric complexities. Nonetheless, their approach required manual parameter measurement, making it less efficient and effective for tools with highly variable cross-sections. Özşahin and Altintas [6] further advanced geometric modelling by developing analytical methods for asymmetric tools and helix angle effects, yet their approach required extensive manual setup. Mancisidor et al. [7] made computational advances using a fixed boundaries approach in combination with Timoshenko beam theory. Nonetheless, considerable challenges persist in accurately modelling the complex contact dynamics between tools and holders.

Tunc [8] introduced a stereolithography (STL) slicing algorithm for modelling cutting tools, enabling accurate calculation of cross-sectional properties directly from 3D models with improved computational efficiency. However, this approach does not fully address variations in tool geometry and materials, such as holder-tool interface, inner cooling channels, and end mills with multiple inserts. Furthermore, cutting tools manufactured using additive techniques, such as those incorporating complex internal cooling channels or lattice structures for thermal management, are also not addressed, underscoring challenges in automatically classifying material transitions, particularly at interfaces between tool bodies and holders composed of different materials.

Most recently, Park et al. [9] introduced a machine learning-based approach that integrates computer vision and convolutional neural networks to predict tool tip dynamics. This methodology reduces dependency on experimental setups by using image-based geometry extraction and trained ML models. While promising in terms of automation and scaling across diverse configurations, it presents challenges such as the need for large datasets and the incorporation of complex material property variations.

Joint contact dynamics modelling at tool-holder and machine-holder interfaces represents another critical aspect of RCSA development. Liao et al. [10] employed fractal theory and Hertz contact mechanics to characterise shrink-fit interfaces, demonstrating how radial interference and tool insertion length affect joint stiffness. However, their model was limited to shrink-fit holders and did not address other interface types. Miao et al. [11] proposed an analytical model incorporating distributed nonlinear spring-damping layers for multiple joint interfaces, including collet-holder connections. While their approach considered translational and rotational motions, they did not fully address the complex nonlinear behaviour at collet interfaces. Schmitz et al. [12] empirically demonstrated that rotation-to-moment stiffness follows a second-order dependence on tool diameter while other stiffness terms remain constant, but the underlying physics of this relationship remains unexplained. These studies highlight a critical need for experimental validation across a broader range of holder configurations. Furthermore, while theoretical frameworks for nonlinear contact dynamics exist, a significant gap remains between these complex models and their practical implementation in industrial settings.

Park et al. [13] first established the importance of rotational degrees of freedom (DOF) in coupling accuracy and proposed an inverse receptance coupling approach using short and long solid carbide rods to extract rotational receptances from direct and cross displacement-to-force measurements. While this method demonstrated that rotational DOF improves tool tip prediction accuracy, the complex mathematical formulations and specificity to tools with the same holder-tool connection geometry have limited its industrial application.

Schmitz et al. [14] incorporated rotational DOF and employed a second-order finite difference approach (FDA) together with the reciprocity principle to obtain the displacement-to-moment (L) and rotation-to-force (N) receptances. They utilised a synthesised formula to estimate the rotation-to-moment (P) receptance, requiring only three translational frequency response functions (FRF) to calculate the full receptance matrix at the tip. However, the synthesised formula introduced some errors in the P component, leading to the occurrence of extra modes and signal distortion, which decreased the accuracy of tool tip predictions [15,16].

Albertelli et al. [15] proposed a second-order FDA to address these issues, requiring nine FRFs. The efficacy of this approach depends on the number of accelerometers [17]. For instance, if three accelerometers are utilised, a single setup is sufficient, requiring only three impact tests. However, this setup adds extra mass to the structure, necessitating additional processing to compensate for this mass and improve prediction accuracy [17]. If only one accelerometer is available, it must be moved to three positions, resulting in nine impact tests. This method is time-consuming, especially when repeated measurements are needed to ensure reliability. Additionally, signal uncertainties are increased due to misalignment between the intended and actual force direction during impact [18].

To compensate for extra modes and signal distortion, Ji et al. [16] introduced an enhanced technique involving two compensation strategies to process data from impact tests. The first compensation strategy conducts modal analysis on the displacement-to-force and displacement-to-moment relationships at the tip to obtain mode information and derive the rotation-to-moment relationship. The second strategy computes and then corrects for extra modes by referencing the displacement-to-force and displacement-to-moment relationships, which do not have extra modes. Although this methodology does not require additional experiments, it is limited by the need for additional signal post-processing, which constrains its applicability in industrial scenarios.

Recent works on determining in-process tool tip dynamics have explored various approaches to overcome static measurement limitations. Wan et al. [19] developed a cutting state-independent method that combines RCSA with operational modal analysis for rotating tool systems, with validation demonstrated on micro-milling applications. Their approach determines in-process poles from cutting tests using non-contact laser sensors for velocity measurements and established signal processing techniques, thereby avoiding impact testing on the rotating tool. Ji et al. [20] developed a frequency-based substructure method for determining rotating tool-tip FRFs by measuring holder-points, later enhancing this with a calibration rod selection strategy [21]. Nevertheless, these methods require physical testing of the specific tool or calibration rods under operating conditions, rather than enabling prediction at the design stage using only the geometric information of the tool.

Thus, it can be seen that significant advancements have been made in RCSA methodologies; however, several critical challenges hinder their

broader adoption. Firstly, the requirement for numerous impact tests and intricate measurement setups renders existing methods impractical for industrial applications. Secondly, the limited expertise in industrial environments to implement complex theoretical models or advanced software further constrains the adoption of these methods. This underscores the need for quick and automated computational approaches that simplify the prediction of tool tip dynamics while maintaining accuracy. Lastly, the absence of automated solutions for modelling the complexity of tool geometries, material variations, and tool-holder interfaces further restricts RCSA applicability in production environments.

This paper, therefore, presents a novel computational approach using RCSA to predict tool tip dynamics, which enhances both theoretical rigor and industrial practicality. The core contribution is a dual approach to dynamic prediction: a simplified first-order finite difference method requiring only three impact tests with a single accelerometer (optimised for industrial deployment). The first-order methodology dramatically reduces implementation complexity and experimental overhead compared to existing approaches. The accuracy of this method is demonstrated by extensive validation across multiple holder types (shrink-fit, collet chuck, hydraulic, and high-power chuck). The theoretical framework is strengthened by an advanced machine learning-assisted slicing algorithm that automates geometric analysis of complex tools directly from STL files automatically identifying components, predicting material properties, and modelling contact stiffness. This automation is enhanced by a comprehensive contact dynamics framework that captures coupling between translational and rotational motion while incorporating frequency-dependent joint behaviour. Together, these advances make reliable prediction of tool tip dynamics more accessible for industrial applications.

2. Methodology description

The methodology proposed in this paper aims to balance accurate prediction with a minimal number of frequency response function (FRF) signals. Additionally, the setup is designed to be straightforward, enabling easy implementation in a production environment with multiple machines, holders, and cutting tools. This approach is also efficient regarding time and cost, enhancing its practicality for industrial applications. The machine-spindle-holder-tool combination is divided into three substructures: machine-spindle-flange (MSF), holder (H) (without flange and taper), and tool (T), as shown in Fig. 1.

The joint between the machine-spindle and the holder is modelled as rigid and the holder and tool joint is modelled by contact stiffness matrix K_{HT}. It should be noted that the holder is considered without the taper and the flange, because for a given spindle, all holders inserted in that spindle will typically have the same flange geometry. In such cases, only the portion of the holder extending beyond the flange varies, as this extension is necessary for automatic tool changes.

The following equations explain how the values described in Fig. 1 are obtained. The proposed methodology is illustrated in Fig. 2, which outlines the steps involved.

1) Obtain the receptance matrix $[G_{33}]_{\text{H1 exp}}$ at the tip (position 3) of the Machine-spindle-flange-holder 1 (MSF-H1) assembly. Three impact tests are required ($H_{3a3a}, H_{3b3b}, H_{3a3b}$), as outlined in subsection 2.1. Follow the guidelines in section 2.3 to determine the spacing between impact positions (s).

$$[G_{33}]_{\text{H1 exp}} = \begin{bmatrix} H_{33} & L_{33} \\ N_{33} & P_{33} \end{bmatrix}_{\text{H1 exp}} \tag{1}$$

2) Obtain the receptance matrix $[G_{11}]_{\text{T1 exp}}$ (position 1) at the tip of the MSF-H1-T1 assembly. Three impact tests are required ($H_{1a1a}, H_{1b1b}, H_{1a1b}$), as outlined in subsection 2.1. Follow the guidelines in section 2.3 to determine the spacing between impact positions (s).

$$[G_{11}]_{T1\ exp} = \begin{bmatrix} H_{11} & L_{11} \\ N_{11} & P_{11} \end{bmatrix}_{T1\ exp} \tag{2}$$

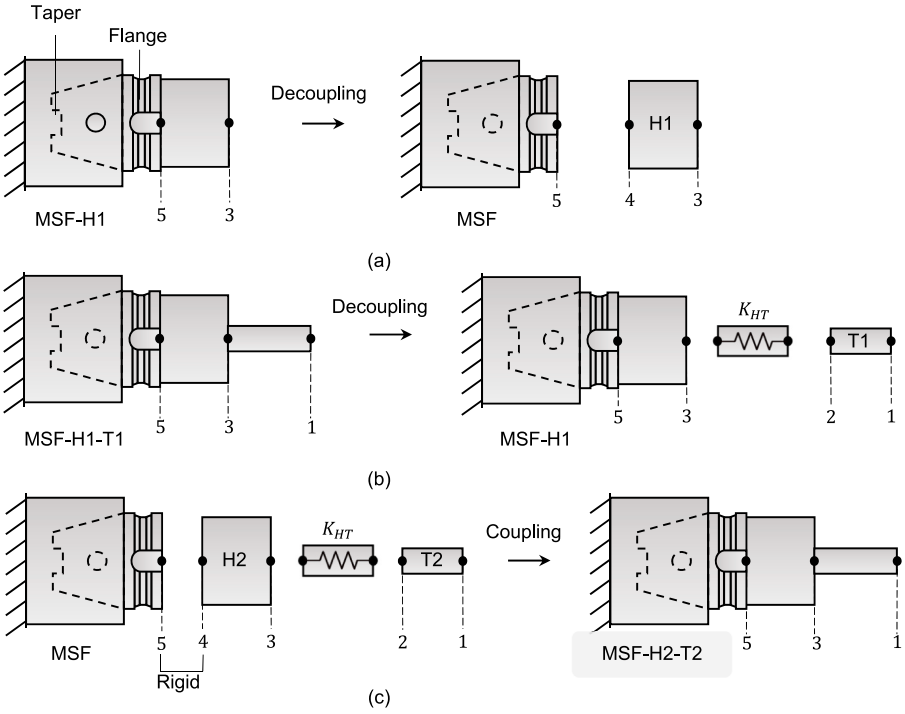

Fig. 1. Spindle-holder-tool substructures and assembly for the proposed computational approach using Receptance Coupling Substructure Analysis (RCSA) to predict tool tip dynamics. (a) Decoupling holder 1 (H1) from the machine-spindle-flange assembly (MSF) to obtain the MSF receptance matrix ($[G_{55}]$). (b) Decoupling tool 1 (T1) from the machine-spindle-flange-holder 1 (MSF-H1) assembly to obtain holder-tool contact stiffness matrix ($[K_{HT}]$). (c) Coupling new tool (T2), with a new holder (H2) and the MSF.

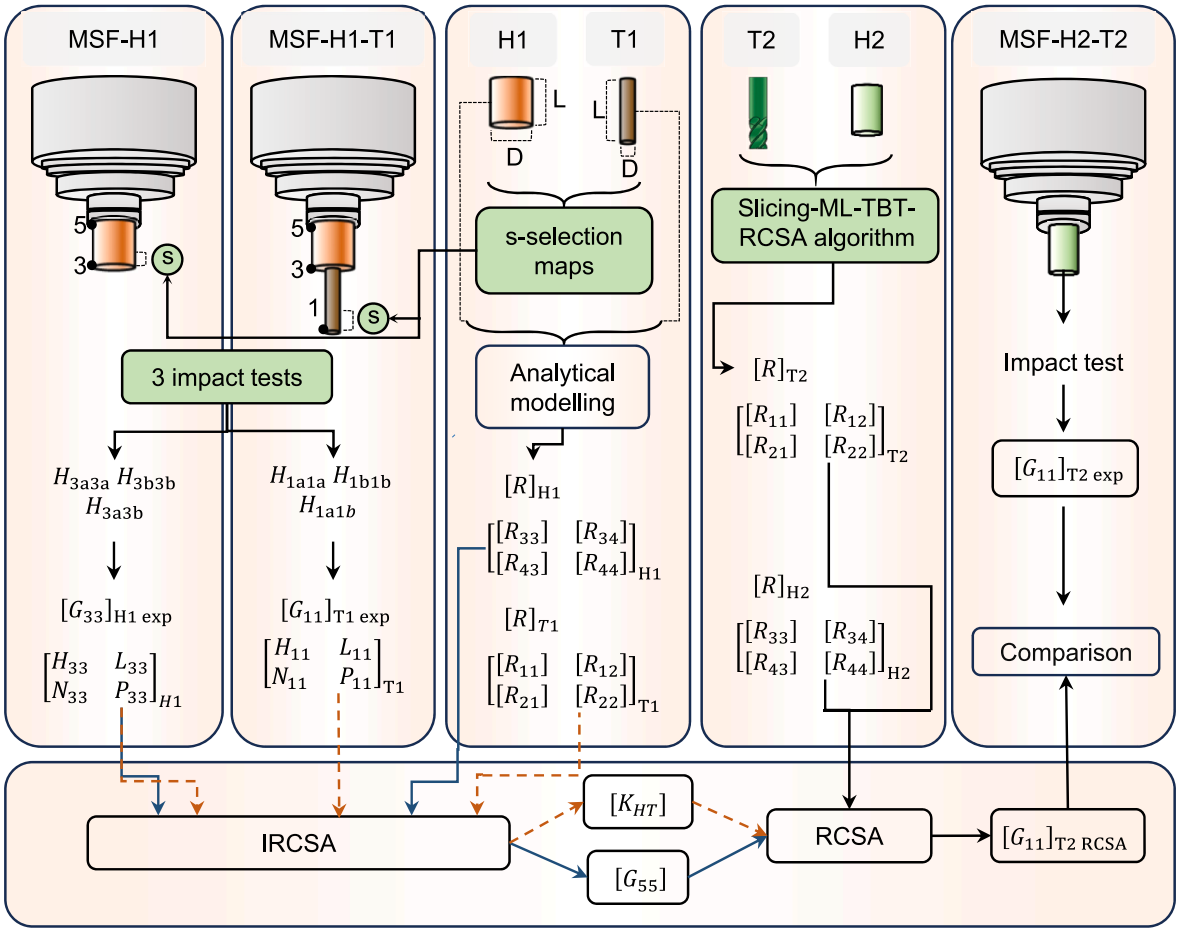

Fig. 2. Proposed methodology to predict tool tip receptance using analytical modelling and Receptance Coupling Substructure Analysis (RCSA). The methodology is presented in a linear fashion, running from left to right. Green boxes represent the main contributions in the proposed methodology. (For interpretation of the references to colour in this figure legend, the reader is referred to the Web version of this article.)

3) Obtain the receptance matrices $[R]_{\mathrm{H1}}$ and $[R]_{\mathrm{T1}}$ for H1 and T1, respectively. The analytical Timoshenko beam theory [4] is used to obtain direct and cross receptances from the substructures.

$$[R]_{\mathrm{H1}} = \begin{bmatrix} [R_{33}] & [R_{34}] \\ [R_{43}] & [R_{44}] \end{bmatrix}_{\mathrm{H1}} \tag{3}$$

$$[R]_{\mathrm{T1}} = \begin{bmatrix} [R_{11}] & [R_{12}] \\ [R_{21}] & [R_{22}] \end{bmatrix}_{\mathrm{T1}} \tag{4}$$

4) Apply IRCSA to determine the MSF receptance matrix $[G_{55}]$. In this step, H1 is decoupled from the MSF assembly, as shown in Fig. 1a. The matrix $[G_{33}]_{\mathrm{H1\ exp}}$ and $[R]_{\mathrm{H1}}$ determined in steps 1 and 3 are used.

$$[G_{55}] = \begin{bmatrix} H_{55} & L_{55} \\ N_{55} & P_{55} \end{bmatrix} = [R_{33}] - [R_{34}] \cdot \left([G_{33}]_{\mathrm{H1\ exp}} + [R_{44}]\right)^{-1} \cdot [R_{43}] \tag{5}$$

5) Apply IRCSA to determine the contact stiffness matrix $[K_{HT}]$. The stiffness and damping terms are defined by their subscripts. The first subscript (x or θ) indicates the direction of motion (translation or rotation), while the second subscript (f or m) denotes the type of loading (force or moment). In this step, T2 is decoupled from the MSF-H1 assembly, as shown in Fig. 1b. The matrices $[G_{11}]_{\mathrm{T1\ exp}}$, $[G_{33}]_{\mathrm{H1\ exp}}$, and $[R]_{\mathrm{T1}}$ are utilised.

$$[K_{HT}]^{-1} = \begin{bmatrix} k_{\mathrm{xf}} + i\omega c_{\mathrm{xf}} & k_{\theta\mathrm{f}} + i\omega c_{\theta\mathrm{f}} \\ k_{\mathrm{xm}} + i\omega c_{\mathrm{xm}} & k_{\theta\mathrm{m}} + i\omega c_{\theta\mathrm{m}} \end{bmatrix}_{HT}^{-1} = \left([R_{12}]_{T1}^{-1} \cdot \left([R_{11}]_{T1} - [G_{11}]_{\mathrm{T1\ exp}}\right) \cdot [R_{21}]_{T1}^{-1}\right)^{-1} - [G_{33}]_{\mathrm{H1\ exp}} - [R_{22}]_{\mathrm{T1}} \tag{6}$$

6) Obtain the receptance matrices $[R]_{\mathrm{T2}}$ and $[R]_{\mathrm{H2}}$ for T2 and H2, respectively. The slicing-ML-TBT-RCSA algorithm detailed in subsection 2.4 is used to obtain direct and cross receptances of substructures T2 and H2.

$$[R]_{\mathrm{T2}} = \begin{bmatrix} [R_{11}] & [R_{12}] \\ [R_{21}] & [R_{22}] \end{bmatrix}_{\mathrm{T2}} \tag{7}$$

$$[R]_{H2} = \begin{bmatrix} [R_{33}] & [R_{34}] \\ [R_{43}] & [R_{44}] \end{bmatrix}_{\mathrm{H2}} \tag{8}$$

7) Predict the tool tip receptance matrix $[G_{11}]_{\mathrm{T2\ RCSA}}$. In this step, the matrices obtained in steps 4, 5, and 6 are utilised.

$$[G_{11}]_{\mathrm{T2\ RCSA}} = \begin{bmatrix} H_{11} & L_{11} \\ N_{11} & P_{11} \end{bmatrix}_{\mathrm{T2\ RCSA}} = [R_{11}]_{\mathrm{T2}} - [R_{12}]_{\mathrm{T2}} \cdot \left([G_{11}]_{\mathrm{T1\ exp}} + [K_{HT}]^{-1} + [R_{22}]_{\mathrm{T2}}\right)^{-1} \cdot [R_{21}]_{\mathrm{T2}} \tag{9}$$

8) An impact test is conducted in the assembly MSF-H2-T2, to obtain its receptance matrix $[G_{11}]_{\mathrm{T2\ exp}}$. Finally, this matrix is compared with the obtained via RCSA in the previous step to complete and validate the prediction.

The proposed methodology offers a streamlined approach, rendering it accessible and easier to implement in an industrial setting. The advantages of this methodology include.

- **Testing efficiency:** only three signals are necessary to derive the full receptance matrix, significantly reducing the number of tests required for each machine, which is advantageous on the shop floor. Additionally, it simplifies the acquisition of the contact stiffness matrix for tools with varied holder-tool geometries.
- **Simplified setup:** conducting the tests requires only three impacts using a single accelerometer. Unlike previous methods, the proposed approach simplifies the experimental procedure, reduces measurement uncertainty, and decreases the number of signals that need to be post-processed.
- **No extra modes:** does not introduce any additional modes, eliminating distortions in the rotation-to-moment receptances. Consequently, it reduces uncertainty in predicting the tool tip dynamics.
- **No extra post-processing:** there is no need for additional post-processing to obtain the full receptance matrix. The proposed methodology inherently handles signal distortions, eliminating the need for further steps to correct or eliminate errors.
- **Modelling efficiency:** ensures time-efficient and accurate free-dynamic modelling without external FEA software by integrating analytical Timoshenko beam equations and RCSA with a ML-slicing algorithm to account for holder-tool geometrical and material details.

It is important to note that whilst this methodology significantly reduces complexity compared to previous approaches, it does not eliminate the need for expertise in the initial dynamic characterisation. Users still require fundamental knowledge of vibration theory, proper experimental setup techniques, and appropriate data interpretation skills for the first characterisation of the machine-spindle receptance matrix and holder-tool contact stiffness. However, once this initial characterisation is completed, the methodology enables users to predict the dynamic behaviour of a wide range of tools without additional experimental testing.

2.1. Full receptance matrix estimation

This section outlines the method to reduce the number of experimental tests while ensuring accurate calculation of the full receptance matrix, including both translational and rotational effects. It should be noted that this procedure is employed to obtain both $[G_{55}]$ and $[K_{HT}]$ using Eqs. (5) and (6), respectively. The proposal is based on Sattinger [22], who showed that the full receptance matrix can be obtained by derivatives of the FRF, as shown in Eq. (10).

$$\begin{Bmatrix} x_i \\ \theta_i \end{Bmatrix} = \begin{bmatrix} H_{ij} & L_{ij} \\ N_{ij} & P_{ij} \end{bmatrix} \begin{Bmatrix} F_j \\ M_j \end{Bmatrix} = \begin{bmatrix} H_{ij} & \dfrac{\partial H_{ij}}{\partial s_2} \\ \dfrac{\partial H_{ij}}{\partial s_1} & \dfrac{\partial^2 H_{ij}}{\partial s_1 \partial s_2} \end{bmatrix} \begin{Bmatrix} F_j \\ M_j \end{Bmatrix} \tag{10}$$

where H_{ij} is the displacement-to-force, L_{ij} the displacement-to-moment, N_{ij} rotation-to-force, and P_{ij} the rotation-to-moment. The subscripts i and j represent the displacement and force position, respectively, at which the receptance is obtained. s_1 is the displacement measurement (e.g., using an accelerometer or laser displacement sensor) and s_2 the distance of the applied force (with the impact hammer) concerning a reference point (Fig. 3). The derivatives are obtained by finite difference approximations (FDA) due to the discrete nature of the experimental tests [23]. The complete mathematical derivation of the full receptance matrix components is provided in Appendix A.

To simplify the procedure and apply the reciprocity principle, Sattinger [22] assumed that the accelerometer measurement position (s_1) and hammer impact position (s_2) should be the same, later denoted as s (measurement spacing). Moreover, as the methodology focusses on the tip receptance matrix, the terms of primary interest are H_{1a1a}, L_{1a1a}, N_{1a1a}, and P_{1a1a}.

The equations used by Schmitz et al. [14], Albertelli et al. [15], and the proposed are compared in Table 1. Based on these equations, Fig. 4 presents the experimental setup used in each methodology, employing

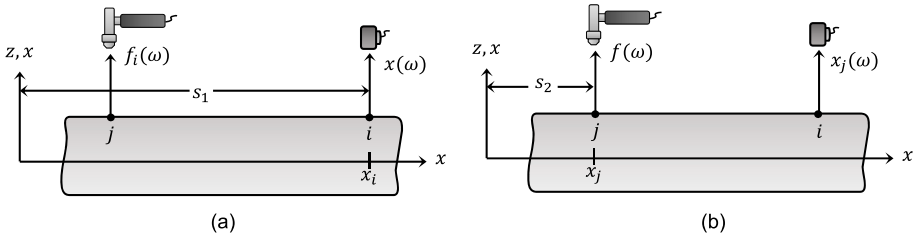

Fig. 3. Receptance Measurement Setup. (a) Force applied at j and displacement measured at i at distance s_1 and (b) displacement measured in i and force applied at j at distance s_2. Both configurations illustrate the experimental setup for determining receptance components. Adapted from Sattinger [22].

Table 1
Comparison of equations to calculate the components of the full receptance matrix.

Albertelli et al. [15]	Schmitz et al. [14]	Proposed
$L_{1a1a} = \frac{3H_{1a1a} - 4H_{1a1b} + H_{1a1c}}{2s}$ $N_{1a1a} = L_{1a1a}$ $L_{1b1a} = \frac{3H_{1b1a} - 4H_{1b1b} + H_{1b1c}}{2s}$ $N_{1a1b} = L_{1b1a}$ $L_{1c1a} = \frac{3H_{1c1a} - 4H_{1c1b} + H_{1c1c}}{2s}$ $N_{1a1c} = L_{1c1a}$ (11)	$L_{1a1a} = 3H_{1a1a} - 4H_{1a1b} + H_{1a1c}$ $N_{1a1a} = L_{1a1a}$ (12)	$L_{1a1a} = \frac{H_{1a1a} - H_{1a1b}}{s}$ $N_{1a1a} = L_{1a1a}$ (13)
$P_{1a1a} = \frac{3L_{1a1a} - 4L_{1b1a} + L_{1c1a}}{2s}$ (14)	$P_{1a1a} = \frac{L_{1a1a}^2}{H_{1a1a}}$ (15)	$P_{1a1a} = \frac{H_{1a1a} - 2H_{1a1b} + H_{1b1b}}{s^2}$ (16)

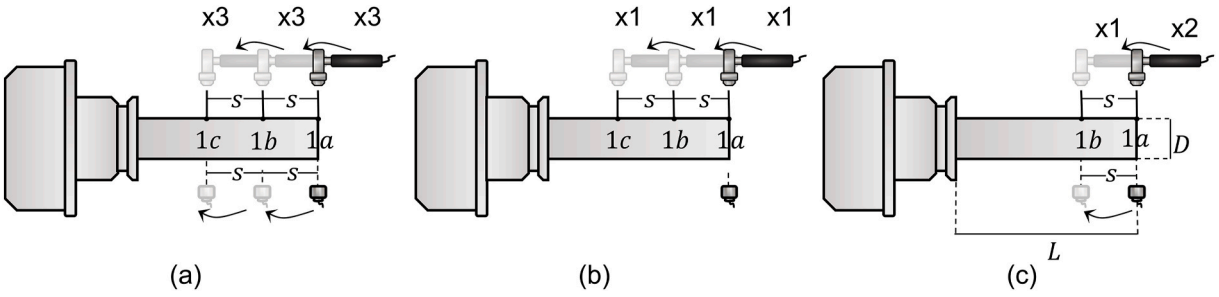

Fig. 4. Experimental test setups for obtaining receptances using (a) Albertelli et al. [15], (b) Schmitz et al. [14], and (c) the proposed methodology. Positions 1*a*, 1*b*, and 1*c* indicate where measurements (displacement or acceleration) and/or impacts are made, with *s* denoting the measurement spacing.

the standard tap-testing equipment (i.e., accelerometer and hammer).

Schmitz et al. [14] employed a second-order FDA to derive the L_{1a1a} and N_{1a1a} terms, as shown in Eq. (12). They also applied the reciprocity principle to establish the equality $L_{1a1a} = N_{1a1a}$ and subsequently used a simplification based on [24] to derive P_{1a1a} using Eq. (15). However, when the denominator H_{1a1a} approaches zero, it introduces a degree of inaccuracy. This situation leads to the appearance of extra modes that distort the P_{1a1a} signal, as illustrated in Fig. 7b.

To address this issue, Albertelli et al. [15] used a second-order FDA to calculate P_{1a1a}, as set out in Eqs. (11) and (14). These equations retain only the measurement spacing s in the denominator, effectively eliminating extra modes. While this approach improves accuracy, it lacks practicality due to the requirement for nine translational frequency response functions (FRFs). These additional FRFs complicate the experimental procedure and increase uncertainty caused by the dispersion of hammer impacts around the ideal excitation points [18]. A theoretical error analysis of the second-order FDA and its sensitivity to measurement uncertainty is detailed in Section 2.2.

To validate the accuracy of the proposed equations (13) and (16), a simplified version of the spindle-holder depicted in Fig. 5a, was analysed. The analytical RCSA Timoshenko beam theory (TBT) formulation proposed by Erturk et al. [4] was used as a reference for comparison, due to it is a closed-form solution. The complex structure was segmented into substructures for individual analysis, as shown in Fig. 5b. Values for bearing dynamics under operational conditions and dynamic properties for interfaces identified by Özşahin et al. [25] were utilised. The tool was excluded from the analysis as the tip of the holder was sufficient for validation purposes.

Fig. 6 illustrates the nine translational FRFs required by the Albertelli et al. [15] methodology, following the setup shown in Fig. 4a. As expected, all vibrational modes exhibit the same natural frequency, but their magnitudes differ. Interestingly, the cross FRFs are identical to their reciprocals (e.g., H_{1a1b} is equal to H_{1b1a}), supporting the use of the reciprocity principle to reduce the number of required FRFs, as shown in Eq. (16).

Fig. 7a illustrates the displacement-to-moment components (L_{1a1a}). Both the first-order FDA (used in the proposed methodology) and the second-order FDA (used by Schmitz et al. [14] and Albertelli et al. [15]) accurately fit the response signal obtained analytically with the RCSA TBT [4]. Although second-order finite differences theoretically have lower truncation error, the practical differences between the two methods are negligible here— peak magnitude error in Fig. 7a is lower than 0.3 %. This small discrepancy is attributed to the appropriate choice of measurement spacing (s), as discussed in Section 2.3

A *significant* characteristic of the proposed methodology is the accuracy of P_{1a1a}. Fig. 7b compares the response of P_{1a1a} across the three methods with the analytical RCSA TBT [4]. The Schmitz et al. [14] methodology reveals additional vibration modes due to the zeros of the FRF (H_{1a1a}), which generate signal distortion. In contrast, the Albertelli et al. [15] method (second-order FDA) and the proposed method (first-order FDA with reciprocity principle) exhibit similar behaviour, closely aligning with the Timoshenko model. Notably, our approach achieves a peak magnitude error of below 0.01 %, demonstrating that a first-order FDA can reach very high accuracy when the measurement spacing (s) is properly selected, as discussed in Section 2.3.

The number of FRFs is also critical. The Albertelli et al. method employs the second-order FDA, initially requiring nine FRFs for implementation. By applying the reciprocity principle, as demonstrated in Eq. (17), this requirement can be reduced to six FRFs without compromising accuracy—a finding validated by the unaltered behaviour of the signal denoted as 'Simplified' in Fig. 7b. Our proposed method utilises first-order FDA, requiring only three FRFs, thus offering a more efficient approach through simplified signal processing and experimental setup.

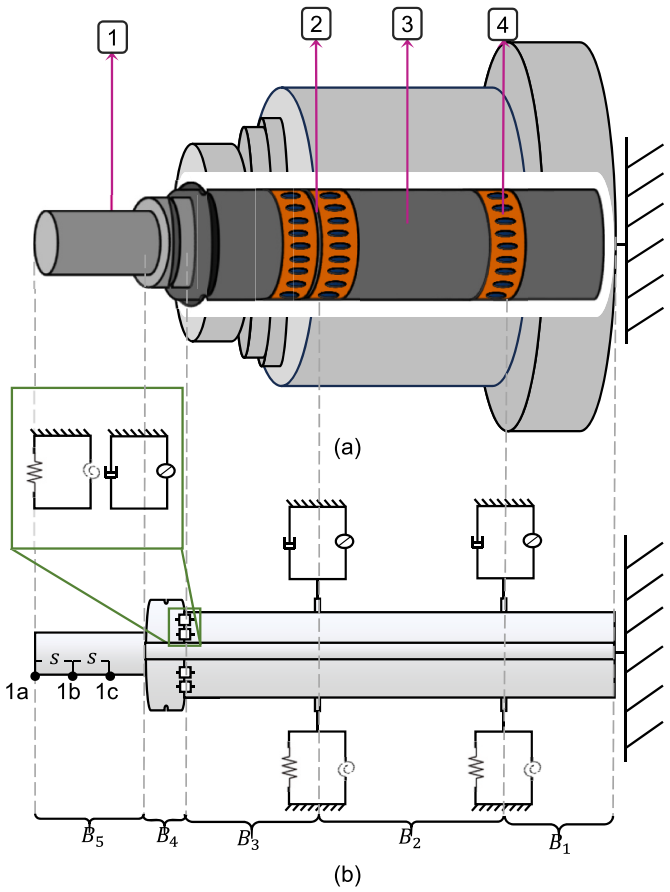

Fig. 5. Spindle-holder-tool assembly: (a) in complex and (b) simplified form using cylindrical beams (denoted as ***B***), interfaces, and bearings. Components labelled: (1) Holder, (2) Front Bearing, (3) Spindle, and (4) Rear Bearing.

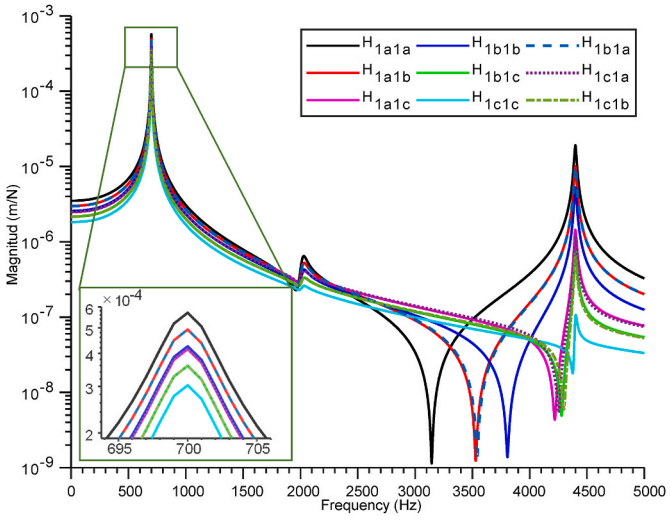

Fig. 6. Translational FRFs obtained analytically. Nine Frequency Response Functions (FRFs) are depicted, as required by the Albertelli et al. [15] methodology. Dashed signals overlap with their reciprocals (e.g., H_{1a1b} with H_{1b1a}) following the reciprocity principle [22]. The subscripts indicate measurement and excitation points: the first number refers to the measurement location, while the second letter denotes the section where the excitation is applied, as illustrated in Fig. 4.

$$P_{1a1a} = \frac{9H_{1a1a} - 24H_{1a1b} + 6H_{1a1c} - 8H_{1b1c} + 16H_{1b1b} + H_{1c1c}}{4s^2} \tag{17}$$

2.2. Truncation errors vs. uncertainty propagation in FDA methods

This subsection presents a theoretical error analysis of finite difference approximation (FDA) methods, establishing general equations for calculating both truncation and uncertainty propagation errors. Inspired by Gibbons et al. [26], we develop a comprehensive mathematical framework that demonstrates how measurement noise amplification can offset theoretical truncation advantages in higher order methods. Rather than revisiting the mass loading effects documented by Ji et al. [27], this analysis establishes optimal measurement spacing criteria and identifies error thresholds where first-order FDA outperforms the second-order for estimating the full receptance matrix.

To establish the mathematical framework for our error analysis, we recall the relationship between translational and rotational degrees of freedom from Eq. (10). Each frequency response function (H_{ij},L_{ij},N_{ij}, and P_{ij}) can be characterised by its mode shapes ϕ_r and their corresponding eigenvalues

$$H_{ij}(\omega) = \sum_{r=1}^{N} \frac{\phi_r(x_i)\phi_r(x_j)}{\omega_r^2 - \omega^2} \tag{18}$$

$$N_{ij}(\omega) = \sum_{r=1}^{N} \frac{\phi_r^{(1)}(x_i)\phi_r(x_j)}{\omega_r^2 - \omega^2} \tag{19}$$

$$L_{ij}(\omega) = \sum_{r=1}^{N} \frac{\phi_r(x_i)\phi_r^{(1)}(x_j)}{\omega_r^2 - \omega^2} \tag{20}$$

$$P_{ij}(\omega) = \sum_{r=1}^{N} \frac{\phi_r^{(1)}(x_i)\phi_r^{(1)}(x_j)}{\omega_r^2 - \omega^2} \tag{21}$$

The subscripts i and j in Eqs. (18)–(21) represent the displacement and force position, respectively, at which the receptance is obtained. N is the total number of measured modes, ω is the excitation frequency, and ω_r is the rth natural frequency. The superscript in the rotational mode shapes $\phi_r^{(1)}$ indicates the first derivative with respect to the spatial coordinate.

2.2.1. Univariate error analysis

For the univariate function $\phi_r(x)$, we approximate the m-th derivative

$$D_s^{(m)}\phi_r(x) = \frac{m!}{s^m} \sum_{i=i_{min}}^{i_{max}} C_i \phi_r(x + is) \tag{22}$$

where x is the coordinate of interest, s is a small spacing on the structure, C_i are the coefficients of the finite difference formula, and ϕ_r has a continuous bounded derivative.

By Taylor's theorem, if ϕ_r has a continuous bounded derivative of sufficient order, the truncation error is bounded by

$$\left|\phi_r^{(m)}(x) - D_s^{(m)}\phi_r(x)\right| \leq Ts^n \parallel \phi_r^{(n+1)} \parallel \tag{23}$$

where $\left\|\phi_r{}^{(n+1)}\right\|$ is the Euclidean norm of the vector $\phi_r^{(n+1)}$, and T is the truncation coefficient that depends on the specific finite difference formula being used.

In practice, measurements inevitably contain errors. Consider the measured mode shape ϕ_{r_m}, which is the sum of the actual mode shape ϕ_r and some measurement perturbation ε_r, as expressed in Eq. (24).

$$\phi_{rm} = \phi_r + \varepsilon_r \tag{24}$$

This perturbation may contain signal noise as well as measurement or curve fitting errors. When a finite difference equation is applied to such data, it is applied to both the mode shape and the perturbation,

giving rise to the propagation error. For any point x in the region of interest

$$|\phi_r(x) - \phi_{rm}(x)| \leq \|\phi_r - \phi_{rm}\| \leq M_r \tag{25}$$

here, $|\phi_r(x) - \phi_{rm}(x)|$ is the Euclidean distance between the vectors ϕ_r and ϕ_{rm}, and M_r is defined as the upper bound on the measurement perturbation. Applying the finite difference operator to the perturbed data

$$D_s^{(m)}\phi_{rm}(x) = D_s^{(m)}\phi_r(x) + D_s^{(m)}\varepsilon_\phi(x) \tag{26}$$

The noise propagation error can be bounded by Eq. (27).

$$\left| D_s^{(m)}\phi_r(x) - D_s^{(m)}\phi_{rm}(x) \right| \leq \frac{m!}{s^m} M_r \sum_{i=i_{min}}^{i_{max}} \left| C_i \right| \tag{27}$$

2.2.2. Total error

The total error is the sum of truncation and propagation errors, as formulated in Eq. (28).

$$e_T = \left| \phi_r^{(m)}(x) - D_s^{(m)}\phi_{rm}(x) \right| \leq T s^n \| \phi_r^{(n+1)} \| + \frac{m!}{s^m} M_r \sum_{i=i_{min}}^{i_{max}} \left| C_i \right| \tag{28}$$

Herein lies the most significant problem when applying finite difference formulae with real data. As $s \to 0$, the truncation error tends to zero, whilst the propagation error tends to infinity and the method becomes unstable.

2.2.3. Optimum spacing

By minimising the upper bound of the total error in Eq. (28), the total error itself will be minimised; therefore, a value of s must be chosen to balance the two terms. Setting the first derivative (with respect to s) of the total error bound to zero.

$$\frac{d}{ds}\left(T s^n \| \phi_r^{(n+1)} \| + \frac{m!}{s^m} M_r \sum_{i=i_{min}}^{i_{max}} \left| C_i \right| \right) = 0$$

$$n T s^{n-1} \| \phi_r^{(n+1)} \| - m \frac{m!}{s^{m+1}} M_r \sum_{i=i_{min}}^{i_{max}} \left| C_i \right| = 0$$

$$s_{min} = \left(\frac{m \cdot m! \cdot M_r \sum_{i=i_{min}}^{i_{max}} \left| C_i \right|}{n T \| \phi_r^{(n+1)} \|} \right)^{\frac{1}{n+m}} \tag{29}$$

For first derivative (m = 1), Eq. (61) simplifies to

$$s_{min} = \left(\frac{M_r \sum_{i=i_{min}}^{i_{max}} \left| C_i \right|}{n T \| \phi_r^{(n+1)} \|} \right)^{\frac{1}{n+1}} \tag{30}$$

The detailed values of the coefficients C_i and the truncation coefficient T for various orders of finite difference schemes are provided in Appendix A.

2.2.4. Bivariate error analysis

For a bivariate function $\phi_r(x_1, x_2)$, we approximate the mixed partial derivative $\phi_r^{(m_1,m_2)}(x_1, x_2)$ using finite differences with spacings s_1 and s_2, as shown in Eq. (31).

$$D_{s_1,s_2}^{(m_1,m_2)}\phi_r(x_1, x_2) = \left(\frac{m_1!}{s_1^{m_1}} \frac{m_2!}{s_2^{m_2}} \right) \sum_{i_1=i_{1,min}}^{i_{1,max}} \sum_{i_2=i_{2,min}}^{i_{2,max}} C_{i_1,i_2} \phi_r(x_1 + i_1 s_1, x_2 + i_2 s_2) \tag{31}$$

where $C_{i1,i2}$ are the coefficients of the bivariate finite difference formula, typically obtained as the outer product of the univariate coefficients. The truncation error for the bivariate case follows similar principles to the univariate case, as expressed in Eq. (32)

$$\left| \phi_r^{(m_1,m_2)}(x_1, x_2) - D_{s_1,s_2}^{(m_1,m_2)}\phi_r(x_1, x_2) \right| \leq T_1 s_1^{n_1} \| \phi_r^{(n_1+1,m_2)} \| + T_2 s_2^{n_2} \| \phi_r^{(m_1,n_2+1)} \| \tag{32}$$

where T_1 and T_2 are truncation coefficients corresponding to the x_1 and x_2 directions, and n_1 and n_2 are the orders of the finite difference approximations in the respective directions.

When working with measured data containing perturbations, the relationship is analogous to Eq. (24)

$$\phi_{rm}(x_1, x_2) = \phi_r(x_1, x_2) + \varepsilon_r(x_1, x_2) \tag{33}$$

where $|\varepsilon_r(x_1, x_2)| \leq M_r$, the propagation error is bounded by Eq. (34).

$$\left| D_{s_1,s_2}^{(m_1,m_2)}\phi_r(x_1, x_2) - D_{s_1,s_2}^{(m_1,m_2)}\phi_{rm}(x_1, x_2) \right| \leq \left(\frac{m_1!}{s_1^{m_1}} \frac{m_2!}{s_2^{m_2}} \right) M_r \sum_{i_1=i_{1,min}}^{i_{1,max}} \sum_{i_2=i_{2,min}}^{i_{2,max}} \left| C_{i_1,i_2} \right| \tag{34}$$

2.2.5. Bivariate total error

The total error for the bivariate case is given by Eq. (35).

$$e_T = \left| \phi_r^{(m_1,m_2)}(x_1, x_2) - D_{s_1,s_2}^{(m_1,m_2)}\phi_{rm}(x_1, x_2) \right| \leq T_1 s_1^{n_1} \| \phi_r^{(n_1+1,m_2)} \| + T_2 s_2^{n_2} \| \phi_r^{(m_1,n_2+1)} \| + \left(\frac{m_1!}{s_1^{m_1}} \frac{m_2!}{s_2^{m_2}} \right) M_r \sum_{i_1=i_{1,min}}^{i_{1,max}} \sum_{i_2=i_{2,min}}^{i_{2,max}} \left| C_{i_1,i_2} \right| \tag{35}$$

For the mixed first derivative ($m_1 = m_2 = 1$) with equal spacing ($s_1 = s_2 = s$) and assuming similar derivative norms, the error simplifies to

$$e_T \leq 2 T s^n \| \phi_r^{(n+1,1)} \| + \frac{M_r}{s^2} \sum_{i_1=i_{1,min}}^{i_{1,max}} \sum_{i_2=i_{2,min}}^{i_{2,max}} \left| C_{i_1,i_2} \right| \tag{36}$$

where T is the common truncation coefficient (listed in Appendix A) and n is the common order of the finite difference approximation in both directions.

2.2.6. Bivariate optimum spacing

To find the optimal spacing that minimises the total error in the bivariate case with equal spacing in both directions, we differentiate Eq. (36) with respect to s and set equal to zero

$$\frac{d}{ds}\left(2 T s^n \| \phi_r^{(n+1,1)} \| + \frac{M_r}{s^2} \sum_{i_1=i_{1,min}}^{i_{1,max}} \sum_{i_2=i_{2,min}}^{i_{2,max}} \left| C_{i_1,i_2} \right| \right) = 0$$

$$2 n T s^{n-1} \| \phi_r^{(n+1,1)} \| - \frac{2 M_r}{s^3} \sum_{i_1=i_{1,min}}^{i_{1,max}} \sum_{i_2=i_{2,min}}^{i_{2,max}} \left| C_{i_1,i_2} \right| = 0$$

$$s_{min} = \left(\frac{M_r \sum_{i_1=i_{1,min}}^{i_{1,max}} \sum_{i_2=i_{2,min}}^{i_{2,max}} \left| C_{i_1,i_2} \right|}{n T \| \phi_r^{(n+1,1)} \|} \right)^{\frac{1}{n+2}} \tag{37}$$

2.2.7. Comparative analysis: first-order vs second-order methods

This section presents a mathematical comparison between first-order and second-order backward finite difference methods for univariate and bivariate cases, identifying conditions where lower-order methods

outperform higher-order methods despite their theoretically higher truncation errors.

2.2.7.1. Univariate case comparison. For the first-order backward difference method, referring to Appendix A, we have $n = 1$, $T = 1/2$, and $\sum |C_i| = 2$. Substituting these values into Eq. (30), the optimum spacing becomes

$$s_{min,1} = \left(\frac{M_r \cdot 2}{1 \cdot (1/2) \cdot \| \phi_r^{(2)} \|} \right)^{\frac{1}{1+1}} = \left(\frac{4M_r}{\| \phi_r^{(2)} \|} \right)^{\frac{1}{2}} \tag{38}$$

At this optimum spacing, the total error from Eq. (28) becomes

$$e_{T,1,min} = \frac{1}{2} s_{min,1} \| \phi_r^{(2)} \| + \frac{2M_r}{s_{min,1}} \tag{39}$$

Substituting Eq. (38) into Eq. (39) and simplifying

$$e_{T,1,min} = 2 \cdot M_r^{\frac{1}{2}} \cdot \| \phi_r^{(2)} \|^{\frac{1}{2}} \tag{40}$$

For the second-order backward difference method, Appendix A gives $n = 2$, $T = 1/3$, and $\sum |C_i| = 4$. Using Eq. (32), the optimum spacing is

$$s_{min,2} = \left(\frac{M_r \cdot 4}{2 \cdot (1/3) \cdot \| \phi_r^{(3)} \|} \right)^{\frac{1}{2+1}} = \left(\frac{6M_r}{\| \phi_r^{(3)} \|} \right)^{\frac{1}{3}} \tag{41}$$

The total error at this optimum spacing is

$$e_{T,2,min} = \frac{1}{3} s_{min,2}^2 \| \phi_r^{(3)} \| + \frac{4M_r}{s_{min,2}} \tag{42}$$

Substituting Eq. (41) into Eq. (42)

$$e_{T,2,min} = 6^{2/3} \cdot M_r^{\frac{2}{3}} \cdot \| \phi_r^{(3)} \|^{\frac{1}{3}} \tag{43}$$

To determine when the first-order method outperforms the second-order method, we require

$$\frac{e_{T,2,min}}{e_{T,1,min}} > 1 \tag{44}$$

Substituting Eqs. (40) and (43) into Eq. (44) and solving to find M_r

$$M_r > \frac{4}{81} \frac{\| \phi_r^{(2)} \|^3}{\| \phi_r^{(3)} \|^2} \tag{45}$$

The previous equations can be further simplified using the assumptions of Euler-Bernoulli beam theory. The governing differential equation for transverse vibrations of a uniform beam is

$$EIy^{(4)}(x) + \rho A y^{(2)}(t) = 0 \tag{46}$$

where E is the Young's modulus, I is the second moment of area, ρ is the material density, A is the cross-sectional area, y is the transverse displacement, x is the spatial coordinate, and t is time. For free vibration at frequency ω, the mode shapes $\phi_r(x)$ satisfy

$$\phi_r{}^{(4)}(x) - \lambda_r^4 \phi_r(x) = 0 \tag{47}$$

where $\lambda_r^4 = (\rho A \omega_3^2)/(EI)$. This allows us to relate higher-order derivatives to the mode shape

$$\phi_r^{(m)} \approx \lambda_r^m \phi_r \tag{48}$$

Using the assumption in Eq. (48) into Eq. (45)

$$M_r > \frac{4}{81} \frac{\| \lambda_r^2 \phi_r \|^3}{\| \lambda_r^3 \phi_r \|^2} \approx \frac{4}{81} \| \phi_r \|$$

$$M_r > 4.94\% \| \phi_r \| \tag{49}$$

Therefore, the first-order backward finite difference method outperforms the second-order method in the univariate case when the measurement perturbation bound exceeds 4.94 % of the mode shape norm.

2.2.7.2. Bivariate case comparison. For the bivariate case, the analysis follows a similar approach but considers spacing in two directions. When both spacings are equal ($s_1 = s_2 = s$) and we seek the mixed first derivative ($m_1 = m_2 = 1$), the optimum spacings can be derived from Eq. (37).

For the first-order bivariate method ($n = 1$), with $T = 1/2$ and $\sum |C_{i1,i2}| = 4$, the optimum spacing is

$$s_{min,1,biv} = \left(\frac{M_r \cdot 4}{1 \cdot (1/2) \cdot \| \phi_r^{(2,1)} \|} \right)^{\frac{1}{1+2}} = \left(\frac{8M_r}{\| \phi_r^{(2,1)} \|} \right)^{\frac{1}{3}} \tag{50}$$

The total error at the optimum spacing in Eq. (50) can be calculated to be

$$e_{T,1,biv,min} = 3 \cdot M_r^{\frac{1}{3}} \cdot \| \phi_r^{(2,1)} \|^{\frac{2}{3}} \tag{51}$$

For the second-order bivariate method ($n = 2$), with $T = 1/3$ and $\sum |C_{i1,i2}| = 16$, the optimum spacing in Eq. (37) becomes

$$s_{min,2,biv} = \left(\frac{M_r \cdot 16}{2 \cdot (1/3) \cdot \| \phi_r^{(3,1)} \|} \right)^{\frac{1}{2+2}} = \left(\frac{24M_r}{\| \phi_r^{(3,1)} \|} \right)^{\frac{1}{4}} \tag{52}$$

With a corresponding total error, replacing Eq. (52) into Eq. (36)

$$e_{T,2,biv,min} = \frac{8\sqrt{6}}{3} \cdot M_r^{\frac{1}{2}} \cdot \| \phi_r^{(3,1)} \|^{\frac{1}{2}} \tag{53}$$

When comparing the ratio of errors between second-order and first-order methods and determining when this ratio exceeds unity as established in Eq. (44) and solving to find M_r

$$M_r > \left(\frac{3\sqrt{6}}{16} \right)^6 \cdot \frac{\| \phi_r^{(2,1)} \|^4}{\| \phi_r^{(3,1)} \|^3} \tag{54}$$

Employing the Euler-Bernoulli beam theory relationships to the bivariate derivatives, where we consider the physical context of experimental modal analysis (with x_1 representing the displacement coordinate and x_2 the force application position), we can establish the relationships

$$\phi_r^{(m+k,n)} = \lambda_r^k \cdot \phi_r^{(m,n)} \tag{55}$$

$$\phi_r^{(m,n+k)} = \lambda_r^k \cdot \phi_r^{(m,n)} \tag{56}$$

where $\phi_r^{(m,n)}$ represents the mixed partial derivative of order m with respect to the first variable, order n with respect to the second variable, and k is the additional order of differentiation with respect to the other variable. Using the assumptions in Eqs. (55) and (56) into Eq. (54)

$$M_r > \left(\frac{3\sqrt{6}}{16} \right)^6 \cdot \frac{\| \phi_r^{(0,1)} \|}{\| \lambda_r \|} \approx \left(\frac{3\sqrt{6}}{16} \right)^6 \| \phi_r^{(0,0)} \|$$

$$M_r > 0.94\% \| \phi_r \| \tag{57}$$

This threshold is lower than in the univariate case, indicating that for bivariate applications such as those involving mixed partial derivatives in frequency response functions, the first-order method becomes advantageous at much lower measurement perturbation levels.

2.2.8. Practical interpretation

The relationship between the measurement perturbation bound (M_r) and the standard deviation of measurements (σ_r) can be established by considering the statistical properties of the measurement error. Assuming that measurement errors follow a normal distribution, it is a

well-established statistical principle that approximately 95 % of the values from a normally distributed variable lie within the range $\mu \pm 2\sigma$, where μ is the mean and σ is the standard deviation.

When considering repeated measurements of mode shapes at any location, the set $\{\varphi_{rm1}(x), \varphi_{rm2}(x), \ldots, \varphi_{rmk}(x)\}$ exhibits approximately normal distribution. Therefore, the measurement perturbation bound can be related to the standard deviation as

$$\| 2\sigma_r \| \leq M_r \tag{58}$$

where σ_r is the standard deviation of the measured mode shapes from their mean. This relationship allows us to express our findings in terms of practically measurable quantities. Therefore, the first-order backward finite difference method outperforms the second-order method in the univariate case when the standard deviation of measurements exceeds 2.47 % of the mode shape norm

$$\sigma_r > 0.0247 \cdot \| \phi_r \| \tag{59}$$

And for the bivariate case, when the 0.47 % is exceeded.

$$\sigma_r > 0.0047 \cdot \| \phi_r \| \tag{60}$$

This analysis has direct implications for tool tip dynamics predictions in machining applications. For accurate characterisation of machine tool dynamics, all four frequency response functions—translational/force (H_{ij}), rotational/force (N_{ij}), translational/moment (L_{ij}), and rotational/moment (P_{ij})—are required. The latter three necessitate spatial derivatives of mode shapes, with L_{ij} and N_{ij} requiring univariate derivatives and P_{ij} requiring bivariate derivatives.

Our findings demonstrate that first-order finite difference methods should be preferred over second-order methods when the standard deviation of measurements exceeds 2.47 % of the mode shape norm for univariate derivatives and just 0.47 % for bivariate derivatives. In practical machine tool testing, these thresholds are frequently exceeded due to sensor placement errors, impact force variations, and environmental factors [18]. Given that the rotational/moment receptance (P_{ij}) is particularly sensitive to measurement errors in its bivariate calculation, the advantage of first-order methods becomes especially pronounced for this crucial component. These finding challenges conventional numerical analysis wisdom, which typically favours higher-order methods.

2.3. Guidelines for selecting measurement spacing (s)

Non-standardised artifacts are commonly used for experimental characterisation of rotational degrees of freedom in machine tool dynamics. For machine dynamics characterisation, a holder-tool serves as a measurement artifact, while a cylindrical bar serves for determining holder-tool interface parameters [12].

A critical consideration in these characterisation methods is the selection of measurement spacing (s) for the finite-difference approximation (FDA), where no consensus exists on its suitable value:

- Schmitz et al. [18] observed that increasing s improved FDA outcomes but noted that proximity to the spindle posed a constraint in signal-to-noise ratio,
- Albertelli et al. [15] described this as a trade-off: while a larger s distance worsens the approximation given by Eqs. (11) and (14), it reduces the impact of experimental uncertainties of the FRF on predicting the tool tip dynamic receptance,
- Gibbons et al. [26] concluded that decreasing the s parameter naturally reduces the numerical error associated with the FDA; however, the method becomes unstable with smaller spacing.

To address these conflicting requirements, this section proposes a systematic approach for selecting suitable measurement spacing based on artifact geometry. The approach utilises non-dimensional parameters

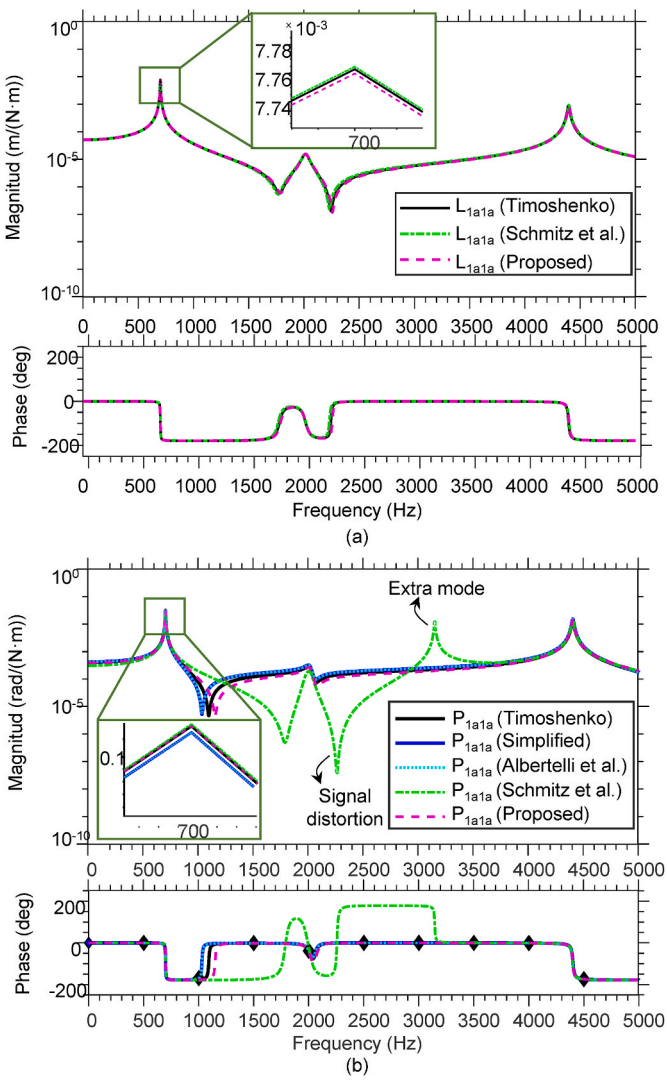

Fig. 7. Comparison of the receptance matrix components calculated by the methods of Schmitz et al. [14] and Albertelli et al. [15], and the proposed method with respect to the Receptance Coupling Substructure Analysis (RCSA) Timoshenko beam model [4]. (a) Displacement-to-moment (L_{1a1a}) and (b) rotation-to-moment (P_{1a1a}) receptances. The simplified Albertelli et al. [15] methodology employing the reciprocity principle is also presented. Y-axis scale is logarithmic.

(s/L and s/D ratios, Fig. 4c), ensuring applicability across varying geometric scales and artifact configurations. This universality makes the methodology a theoretical foundation for characterising tool-holder interfaces and machine head receptance matrices.

The method employs the analytical solution of Timoshenko beam equations with basic inputs: geometric parameters (L, D, s), material properties (density, Young's modulus, and Poisson's ratio) and boundary conditions. Unlike finite element method (FEM) simulations, this analytical approach enables rapid computation across a wide parameter space, facilitating detailed s-selection map construction.

The maps are based on relative error calculations using Eqs. (61) and (62), where the subscript r corresponds to the vibration mode being analysed, M represents the peak magnitude for the vibration mode, and T corresponds to the RCSA Timoshenko beam model [4]. The analysis uses the machine-spindle-holder assembly simplification presented in Fig. 5b.

$$\%Error\ M(L_{1a1a})_r = \frac{\left| M\left(L^T_{1a1a}\right)_r - M\left(L^{FDA}_{1a1a}\right) \right|}{M\left(L^T_{1a1a}\right)_r} \cdot 100 \tag{61}$$

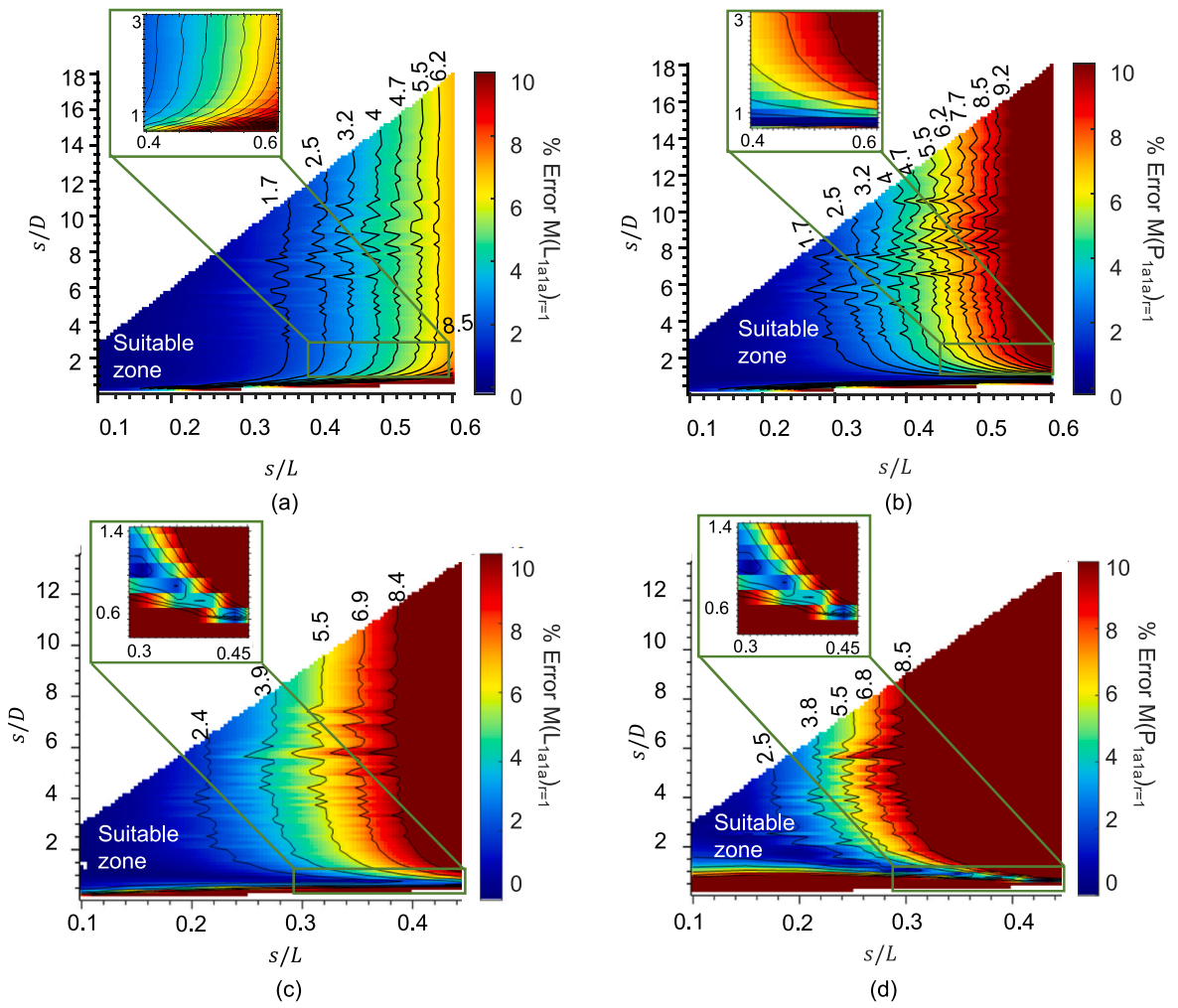

Fig. 8. Selection maps for the measurement spacing position s in relation to the length and outer diameter of the holder. (a) and (b) show the s-selection maps obtained using the first-order finite difference approximation (FDA), while (c) and (d) present the results using the second-order FDA. The "suitable zone" highlights the regions where the measurement spacing s ensures minimal error in the estimation of the receptance components.

$$\%Error\ M(P_{1a1a})_r = \frac{\left|M(P^T_{1a1a})_r - M(P^{FDA}_{1a1a})\right|}{M(P^T_{1a1a})_r} \cdot 100 \tag{62}$$

Fig. 8 presents comprehensive s-selection maps for both first order (Fig. 8a and b) and second order (Fig. 8c and d) finite difference approximations, enabling direct comparison of their respective suitable measurement zones. For each approximation order, maps are provided for both the displacement-to-moment (L_{1a1a}) and the more sensitive rotation-to-moment (P_{1a1a}) receptance terms.

In all maps, a suitable zone is defined as a region where the relative error remains below 2 %, considered acceptable for rotational degrees of freedom estimation in RCSA. Comparing first-order and second-order maps reveals distinct differences in both the size and shape of these suitable zones. The first-order FDA maps exhibit wider suitable zones extending from approximately $0.1L < s < 0.5L$ with respect to length and $0.5D < s < 8D$ with respect to diameter. In contrast, the second-order FDA maps show more constrained suitable zones, particularly for the critical P_{1a1a} receptance component, with suitable regions limited to approximately $0.1L < s < 0.3L$ and $1D < s < 8D$.

The second-order maps demonstrate not only narrower suitable zones but also steeper error gradients outside these zones, indicating greater sensitivity to non-suitable spacing selections. This seemingly counterintuitive behaviour can be explained by examining the mathematical foundation of finite difference approximations when applied to the Timoshenko beam solution.

For the Timoshenko beam, the dynamic transverse deflection for the r-th vibration mode is represented by

$$\phi_r(\bar{x}) = A_r\left[C_1\, sin(\alpha_r \cdot \bar{x}) + C_2\, cos(\alpha_r \cdot \bar{x}) + C_3\, sin\, h(\beta_r \cdot \bar{x}) + C_4\, cos\, h(\beta_r \cdot \bar{x})\right] \tag{63}$$

where the position is represented relative to the length of the beam as $\bar{x} = x/L$. A_r is a constant obtained from mass normalisation of the eigenfunctions. C_1, C_2, C_3, and C_4 are coefficients determined by the boundary conditions. The parameters α_r and β_r are dimensionless frequency numbers that depend on the physical and geometric properties of the beam, including diameter, length, density, Young's modulus, and Poisson's ratio [4].

Standard truncation error analysis establishes that for small normalised step sizes $\bar{s} = s/L$, the second-order backward finite difference approximation (FDA) ensures superior accuracy. The error is proportional to $(\bar{s}^2/3)\,\phi_r^{(3)}(\bar{x})$ with $O(\bar{s}^2)$ truncation error, while the first-order error is proportional to $(\bar{s}/2)\,\phi_r^{(2)}(\bar{x})$ with $O(\bar{s})$ truncation error. However, the accuracy advantage of the second-order method diminishes and can be reversed as $\bar{s}$ increases beyond specific thresholds relative to the characteristic variations within $\phi_r(\bar{x})$.

This reversal can be explained because the derivation of FDA relies on Taylor series expansions, where the error is represented by the first neglected term and higher-order terms. For large $\bar{s}$, these higher-order terms, which are ignored in the leading error term analysis, become

dominant. The n-th derivative of $\phi_r(\bar{x})$ from Eq. (63), denoted $\phi_r^{(n)}$, contains terms with factors such as $C_1\propto_r^{(n)}$, $C_2\propto_r^{(n)}$, $C_3\beta_r^{(n)}$, and $C_4\beta_r^{(n)}$. When $\bar{s}$ is large, contributions from these higher derivatives (e.g., $\phi_r^{(4)}$, $\phi_r^{(5)}$) multiplied by corresponding powers of $\bar{s}$ (e.g., $\bar{s}^4$, $\bar{s}^5$) constitute the significant portion of the error, rather than the leading order term alone.

The parameters $\propto_r$ and β_r in Eq. (63) govern the spatial frequency of trigonometric terms and the rate of change of hyperbolic terms, respectively. Finite difference methods essentially approximate the function $\phi_r(\bar{x})$ with a polynomial over the sampling points. The first-order FDA uses the interval $(\bar{x}_{1-\bar{s}}, \bar{x}_1)$, whilst the second-order FDA uses the wider interval $(\bar{x}_{1-2\bar{s}}, \bar{x}_1)$. As $\bar{s}$ becomes large relative to the wavelengths implicitly defined by $\propto_r$ or the characteristic lengths of hyperbolic variation from β_r, the assumption that $\phi_r(\bar{x})$ behaves as a low-order polynomial over the sampling interval breaks down. The second-order method is more prone to error amplification because it has to maintain fidelity over a wider $2\bar{s}$, as opposed to the linear approximation of the first-order method, which maintains fidelity over a narrower $\bar{s}$ interval. This phenomenon aligns with observations by Hafez et al. [28], who noted similar behaviour in transonic flow calculations. According to their findings, theoretically more accurate second-order schemes failed to converge reliably in practice, while superior numerical robustness was demonstrated by simpler first-order schemes.

The case of rotation-to-moment receptance (P_{1a1a}) is particularly challenging as it involves bivariate derivatives. As shown in Eq. (21), the rotation-to-moment (P_{ij}) receptance involves the product of first derivatives of the mode shape with respect to each spatial variable. The error propagation in bivariate FDA is greater because errors from both directions compound multiplicatively rather than additively. This explains why the suitable zone for P_{1a1a} is more constrained than for L_{1a1a}, particularly in the second-order FDA maps shown in Fig. 8d.

A different numerical issue arises when the measurement spacing position (s) is set too small. For very small values of s, the frequency response functions H_{1a1a} and H_{1a1b} become almost identical. The numerator term ($H_{1a1a} - H_{1a1b}$) in Eq. (13) approaches zero, and with s being small by definition, this ratio becomes mathematically unstable. This establishes a lower bound for the measurement spacing required to maintain numerical stability in finite difference calculations. This mathematical instability manifests physically as erratic predictions of rotational degrees of freedom, leading to unreliable estimates of the full receptance matrix and consequently inaccurate tool tip dynamics predictions. The s-selection maps in Fig. 8 illustrate this effect, with errors increasing dramatically as s/D and s/L approach zero, thus providing a practical lower bound for measurement spacing to ensure numerical stability in the finite difference calculations.

From this preliminary analysis, it is concluded that the measurement spacing position (s) must be selected according to the dimensions (length and diameter) of the holder and tool (Fig. 4c). The proposed selection maps serve as a guide for this determination. The objective is to minimise the error; therefore, s/L and s/D ratios within the suitable zone (less than 2 % error) in Fig. 8 are considered accurate. When geometric constraints prevent selecting measurement positions within this suitable zone, users should be aware that prediction accuracy will be reduced as indicated by the contour lines. These locally introduced errors subsequently propagate through the receptance coupling equations and impacting in the accuracy of the predicted tool tip dynamics.

2.4. Free-free dynamic modelling of cutting tools

This section presents an innovative algorithm for accurate and computationally efficient free-free dynamic modelling of complex multi-material cutting tools. Building on existing methods [8] it combines an enhanced stereolithographic (STL) slicing algorithm with machine learning (ML) techniques to accurately determine material and geometric variations along the length of the cutting tool. The free-free dynamic response is obtained using Timoshenko beam theory (TBT) and receptance coupling substructure analysis (RCSA). The implementation involves the steps outlined in Fig. 9.

2.4.1. Data collection

A comprehensive training dataset that trains the model is established to recognise and classify tool components and their properties. The data collection process consists of three main elements.

- STL Collection: 3D STL geometries of cutting tools are stored in a database. The cutting tools are classified according to their structural family (e.g., shrink-fit holders, monoblock tools). This classification methodology optimises the training process by creating well-defined subsets of similar geometric characteristics. The dataset requires a minimum of 10 representative cutting tools per family to ensure sufficient data for model development and validation.
- Geometric Processing: each 3D STL model is processed using a slicing algorithm that generates cross-sectional slices along the longitudinal axis of the cutting tool, preserving closed contours, and vertex coordinates. Recommended slice heights range from 0.5 to 8 mm, depending on the complexity of the cutting tool. For each resulting slice, the algorithm extracts key geometric properties including the area, perimeter, moment of inertia values (I_x, I_y, and I_{xy}), aspect ratio, relative position within the tool, and curvature characteristics.

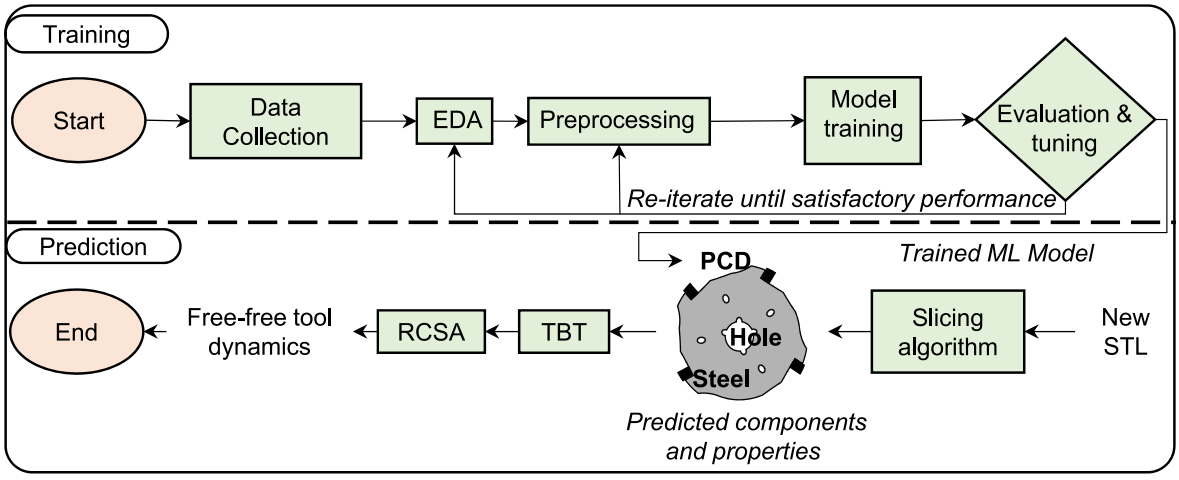

Fig. 9. Workflow of the slicing and machine learning-based algorithm for free-free dynamic modelling of cutting tools, where the tool geometry and materials are predicted and used for analytical dynamic analysis.

- Component Labelling: each geometric feature in the slices is manually labelled with a specific component type: body, holder, channel (cooling channels), or insert. Together with these labels, the geometric features—such as area, moments of inertia, perimeter, aspect ratio, and position—are assigned to the corresponding component.

The detailed mathematical formulations for the STL slicing and geometric feature extraction are provided in Appendix B.

2.4.2. Exploratory data analysis (EDA)

Exploratory data analysis is performed on the labelled dataset, including.

- Null Analysis: identifying and addressing missing values to ensure data completeness.
- Class Distribution Analysis: examining the distribution of component classes to ensure balanced representation.
- Correlation Analysis: understanding the underlying patterns and relationships between features.

2.4.3. Data preprocessing

Exploratory data analysis is performed on the labelled dataset to understand patterns and relationships. This step involves the following tasks.

- Data Balancing: ensuring equal representation of all labels/classes. This step addresses any imbalances identified during EDA.
- Null Imputation: handling missing values using appropriate imputation strategies based on the feature characteristics.
- Normalisation: standardising the data to equalise the contribution of features with different scales. For example, z-score normalisation can transform features to have zero mean and unit variance.
- Feature Selection: identifying the most relevant features for the model. For example, chi-square statistical analysis with significance level thresholds ($\alpha \leq 0.05$) can help select discriminative features.
- Feature Engineering: computing the resultant geometrical, mechanical, and physical properties of each slice. This process begins with material assignment, where appropriate materials are designated to each identified component. Mechanical and physical properties such as density, Poisson's ratio, solid damping factor, shear correction factor, and Young's modulus are assigned. Following this, the mixing law is applied to integrate these properties, resulting in the final geometrical, mechanical, and physical attributes for each slice.

The mathematical details of feature selection and feature engineering are provided in Appendix C.

2.4.4. Model training

A machine learning model is trained using the prepared dataset to predict the slices properties. This step involves the following tasks.

- **Algorithm selection**: evaluating several classification algorithms to determine optimal performance. Examples include Support Vector Machines (SVMs), Random Forests, Neural Networks, or ensemble methods.
- **Hyperparameter optimisation**: identifying optimal values for model parameters. Grid search with cross-validation techniques can efficiently explore the parameter space.
  - **Training protocol**: implementing robust validation methods to ensure model reliability. Cross-validation with minimum 5-fold implementation and accuracy thresholds exceeding 95 % helps confirm model effectiveness.

2.4.5. Model evaluation and tuning

The model is validated using appropriate metrics and fine-tuned hyperparameters to optimise performance.

- **Performance metrics**: calculating multiple metrics to assess model quality. Accuracy, precision, recall, and F1-score for each component class help identify strengths and weaknesses, with particular attention to minimising false positives.
- **Confusion matrix Analysis**: analysing misclassifications to identify patterns. This analysis reveals opportunities for targeted improvements.
- **Iterative refinement**: refining the model through successive iterations, adjusting hyperparameters, feature engineering techniques, and preprocessing steps until satisfactory performance is achieved.

The iteration process continues until classification accuracy exceeds 95 % across all component types, with special emphasis on correctly identifying material transitions.

2.4.6. Tool dynamics prediction

Once the model is trained, evaluated, and tuned, it can be used to make predictions on new data.

- **STL processing**: processing a new cutting tool in STL format using the slicing algorithm to obtain geometric features of each slice.
- **Component classification**: using the trained machine learning model to predict the component type for each contour in every slice, assigning appropriate material properties.
- **Material property integration**: computing effective mechanical and physical properties for each slice using the mixing law, accounting for the spatial distribution of different materials.
- **Timoshenko beam modelling**: considering each slice as a uniform free-free beam, and obtaining the receptance matrices using the analytical Timoshenko beam equations [4], with appropriate shear correction factors derived from Hutchinson's formulations [29].
- **Computational optimisation**: transforming consecutive slices with equal geometry as a single highest slice for saving computational time without sacrificing accuracy.
- **RCSA Implementation**: using the RCSA equations for coupling free-free beams to couple the slices and determine the dynamics of the entire cutting tool, incorporating the diameter-dependent and length-dependent stiffness matrix for holder-tool interactions.

2.4.7. Comparison with other machine learning approaches

The proposed Slicing-ML-TBT-RCSA algorithm automates free-free dynamics prediction for complex cutting tools. It autonomously processes multi-material tools with intricate geometries directly from STL files, eliminating the need for manual geometric interpretation or specialist expertise. This automation significantly reduces the time required for dynamic analysis whilst maintaining prediction accuracy across diverse cutting tool configurations. The advantages of this algorithm include.

1. **Automated workflow:** direct processing of STL files eliminates all manual intervention, from initial geometry processing to final dynamic prediction. The system automatically identifies and classifies components (e.g., inserts, cooling channels, material transitions), ensuring consistent analysis.
2. **Advanced geometric processing:** handles complex modern tool geometries including variable cross-sections, multiple inserts, and internal features through ML-based component recognition. This enables accurate modelling of intricate multi-material tools without geometric simplification or manual pre-processing.
3. **Computational efficiency:** integrates Timoshenko beam theory with ML-driven material property prediction to deliver rapid free-free dynamics characterisation. The algorithm processes complex

tools in seconds by combining analytical solutions with automated slice coupling, eliminating the computational overhead of traditional finite element analysis whilst maintaining prediction accuracy.
4. **Lower computational demands:** the supervised learning approach requires less computational resources for training compared to deep learning techniques.
5. **Effective with small datasets:** the approach functions effectively with smaller, specialised datasets, which is particularly valuable when experimental data collection is resource-intensive.

Our algorithm fundamentally differs from conventional machine learning approaches by implementing a geometry-first methodology that enables direct processing of 3D tool representations. This creates a more robust pathway from design to dynamic analysis than approaches that rely on derived features or simplified parameters.

The most closely aligned work is that of Park et al. [30], who introduced an ML-based RCSA technique that trains convolutional neural networks to predict tool tip FRFs and stability lobes. Whilst both approaches aim to automate FRF modelling for arbitrary tool configurations, the method of Park et al. relies on derived features or simulations, whereas our Slicing-ML-TBT-RCSA algorithm directly leverages the full 3D geometry of the tool. This represents a significant advancement in feature extraction methodology.

When compared to other physics-informed approaches such as that described by Lechner et al. [31] for freeform bending, our algorithm applies beam theory after component identification rather than embedding it directly into the neural network architecture. This allows for more explicit modelling of the physical behaviour and enables greater flexibility in handling complex geometries.

The unique integration of geometric processing, machine learning classification, and physics-based dynamic modelling positions the Slicing-ML-TBT-RCSA algorithm as particularly valuable for applications where 3D geometry must be understood in terms of its structural and dynamic properties. By automating the entire workflow from STL processing to dynamic prediction, our approach eliminates manual intervention whilst maintaining computational efficiency and accuracy across diverse cutting tool configurations.

3. Methodology validation

The methodology was validated using two distinct approaches: i) comparing results against established methods in the literature, and ii) assessing its predictive capabilities across a diverse range of cutting tools.

3.1. Materials and experiments

To compare the proposed methodology with existing approaches, experimental validation through tap-testing was conducted using three setups (Fig. 10), following the workflow outlined in Fig. 2. The first setup (Fig. 10a), used to obtain the spindle-holder receptance matrix $[G_{55}]$ and compare the methods listed in Table 1, consisted of a cylindrical holder (H1) with a 42 mm outer diameter, 12 mm inner diameter, and length 60 mm (without the flange). A measuring spacing s of 25 mm was selected, corresponding to an $\%Error\ M(P_{1a1a})_{r=1}$ of 1.7 % in the s-selection map of Fig. 8b and $\%Error\ M(P_{1a1a})_{r=1}$ of 1.8 % in the s-selection map of Fig. 8d. This distance was selected for a fair comparison of the methodologies.

The second setup (Fig. 10b) was to obtain the contact stiffness matrix $[K_{HT}]$ for the holder-tool joint. This configuration employed a solid carbide bar (T1) with diameter of 12 mm and a length of 100 mm. In this case, the inner diameter matched that of the bar, allowing the continued use of holder H1 from the previous setup. A measuring spacing s of 25 mm was selected, corresponding to an $\%Error\ M(P_{1a1a})_{r=1}$ of 1.1 % in the s-selection map of Fig. 8b and $\%Error\ M(P_{1a1a})_{r=1}$ of 0.8 % in the s-selection map of Fig. 8d. Subsequently, the contact stiffness matrix between the holder and the tool was obtained using IRCSA with Eq. (5).

The third setup (Fig. 10c) was implemented to predict tool tip dynamics of a new tool (T2) and holder (H2) configuration used in a real industrial application. The carbide tungsten cutting tool had four teeth, a diameter of 10 mm in the cutting zone, and a conical shank varying from 10 to 12 mm with 1° of inclination. The thermal tapered HSK-63A shrink holder had an inner diameter of 12 mm and an outer diameter varying from 24 to 32 mm along a length of 90 mm in the tapered zone.

To validate the predictive capabilities across a wide range of cutting tools, multiple holder-tool configurations were tested. Fig. 11a–d illustrates the same solid carbide tungsten tool (T3) mounted in four holder types: high-power (H3, 79 mm length), hydraulic (H4, 73 mm length), collet (H5, 67 mm length), and shrink-fit (H6, 54 mm length). Fig. 11e presents a shell-end milling cutter with five indexable - carbide inserts (T4). Fig. 11f features a monoblock tool (T5) with 36 brazed PCD inserts arranged in nine levels.

A systematic study of the contact stiffness matrix was conducted using solid carbide bars of varying diameters (20, 18, 16, 12, and 10

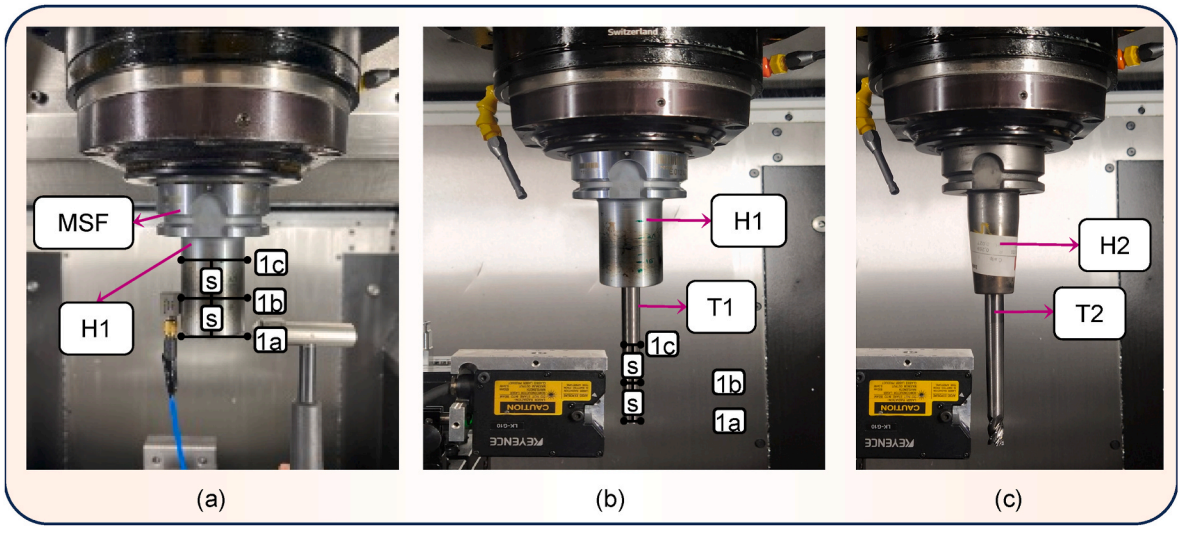

Fig. 10. Experimental setups used to compare the proposed and existing methodologies. (a) Machine-spindle-flange and Holder 1 (H1) setup for characterising the machine–holder interface, (b) Holder 1 (H1) and Tool 1 (T1) setup for measuring contact stiffness at the holder–tool interface, (c) Holder 2 (H2) and Tool 2 (T2) setup used for validating the prediction.

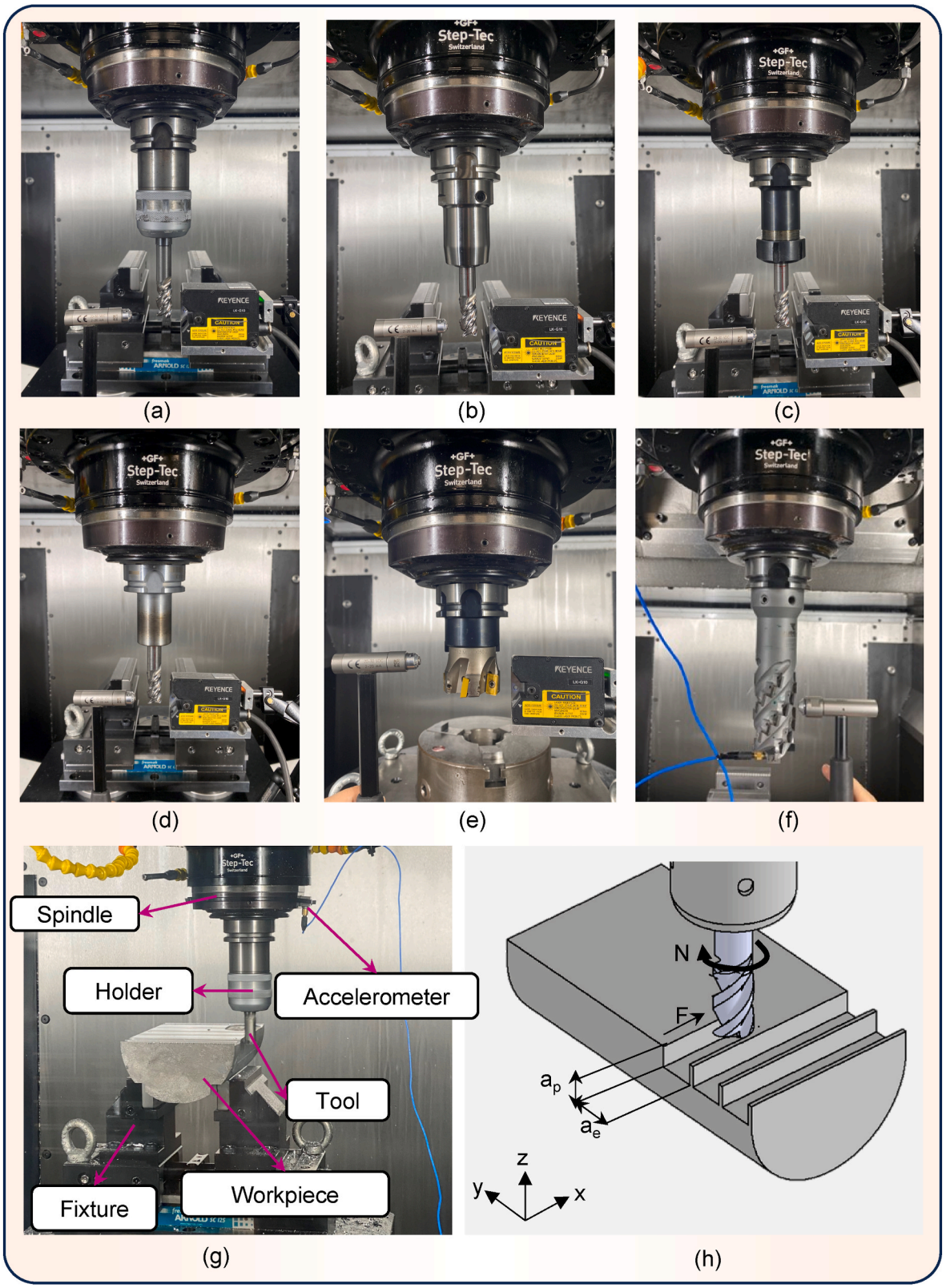

Fig. 11. Experimental validation setups: (a–d) Tool T3 mounted in holders 3 to 6 (H3-H6), respectively; (e) Shell-end mill (T4); (f) Monoblock tool (T5); (g) Complete machining setup with labelled components; (h) Schematic representation of cutting directions and force components.

mm) installed in the four studied holder-tool configurations. Each holder-tool configuration was tested under identical conditions to enable direct comparison of their dynamic characteristics (Fig. 10b). The tool tip receptance data was then used to determine the contact stiffness parameters enabling quantitative comparison of holder interface characteristics.

Finally, to validate the chatter-free machining predictions, down-milling tests were conducted on an A356 aluminium block

($k_s = 1000$ MPa [32]) in a GF P800 U machining centre. The modal parameters of the main vibration modes -both predicted and obtained by tap-testing- were used to construct stability lobe diagrams (SLDs). Different radial depths of cut and axial depths of cut were tested, maintaining a constant feed rate per tooth of 0.1 mm. The machining setup is illustrated in Fig. 11g and, Fig. 11h shows the cutting directions. The chatter occurrence was detected using external (accelerometer and microphone) and internal (signals of the machine) sensors [33].

Tap-testing signals were acquired using DeltaTron type 4525-B triaxial accelerometers and an impact hammer type 8206, both manufactured by Brüel & Kjaer. Due to spatial constraints for accelerometers, alternative measurement methods were employed. Specifically, carbide tungsten tools were assessed using a Keyence LK-G10 laser displacement sensor. This approach also served as dual purpose. It facilitated the validation of the effect of different sensors on predictive lability, thus ensuring comprehensive and robust results. For each test, five tap tests repetitions were performed, and coherence plots were generated to validate signal quality [34].

3.2. Determination of machine-spindle receptance matrix

The proposed methodology was subjected to a comparative analysis along with the methodologies presented in Table 1 to determine the machine-spindle receptance. In particular, the discrepancies in the methodologies employed for calculating the P_{55} component are noteworthy. While first-order finite difference approximations theoretically have larger truncation errors than second-order methods, our experimental validation reveals that practical accuracy depends more strongly on measurement reliability than theoretical error order.

As illustrated in Fig. 12, the P_{55} receptance exhibits a notable degree of signal distortion within the frequency range of 1500–2000 Hz when employing the Schmitz et al. [14] equations. The emergence of additional modes can be associated with the denominator H_{55} approaching zero.

In comparison to the proposed methodology, the Albertelli et al. [15] equations demonstrate a discrepancy in magnitude. The curve obtained with the proposed methodology serves as a reference, as it is also well

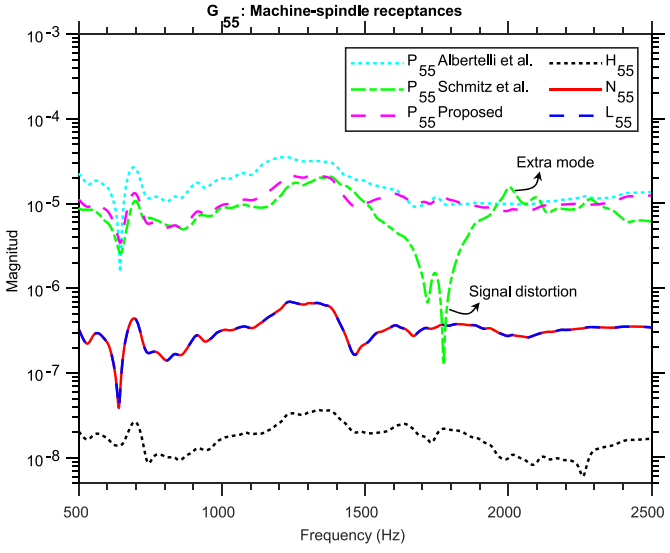

Fig. 12. Machine–spindle–flange (MSF) dynamic response, expressed as receptances (G_{55}), obtained from the experimental setup in Fig. 10a. Results are compared against existing methods from Albertelli et al., Schmitz et al., and the proposed methodology, highlighting signal distortion and an extra mode in the comparison. The receptance components shown are: H_{55} (displacement-to-force, m/N), L_{55} (displacement-to-moment, m/(N·m)), N_{55} (rotation-to-force, rad/N), and P_{55} (rotation-to-moment, rad/(N·m)), all plotted on a logarithmic scale.

aligned with the equations of Schmitz in the range of 500–1300 Hz, where signal distortion does not occur. The discrepancies observed can be attributed to the experimental uncertainty generated by the acquisition of nine FRFs, which is a consequence of the presence of random and systematic errors in the tap-testing methodology [18]. This observation aligns with the theoretical error analysis presented in Section 2.2, which mathematically demonstrates how measurement uncertainties propagate more severely in higher-order finite difference methods. For instance, uncertainty may arise due to misalignment between the predicted and actual force direction during impact. For instance, uncertainty may arise due to misalignment between the predicted and actual force direction during impact.

These experimental findings demonstrate that while higher-order approximations may offer theoretical advantages, practical accuracy is more strongly influenced by measurement methodology reliability than mathematical order of approximation.

3.3. Holder-tool contact stiffness matrix

Having demonstrated the advantages of the proposed equations, the contact stiffness matrix between the holder and the tool was determined. The dynamic properties of the interface obtained using the proposed method are shown in Table 2. The order of magnitude is consistent with the stiffness and damping properties of tungsten carbide cutting tools mounted in thermally tapered HSK-63A shrink holders of the dimensions used, as presented in previous works [4,35].

Upon comparison, no significant differences were observed between the results obtained from the proposed method and those from Albertelli et al. and Schmitz et al. All methodologies provide similar estimations of the dynamic properties of the holder-tool interface, with no notable advantage or relevant discrepancies in the predicted stiffness or damping parameters. This consistency suggests that the proposed equations are equally effective in characterising the interface dynamics while maintaining alignment with established methods.

The experimental study of joint stiffness parameters across various holder-tool configurations revealed distinct characteristics in their mechanical behaviour. Fig. 13 illustrates the relationship between tool diameter and stiffness parameters for four different holder types. The linear displacement-to-force stiffness (K_{xf}) shown in Fig. 13a demonstrates an exponential trend, with values ranging from 10^7 to 10^8 N/m, where shrink-fit holders consistently exhibit superior stiffness across all diameters. Fig. 13b presents the linear displacement-to-moment stiffness (K_{xm}), which shows more moderate variation with diameter, maintaining values in the order of 10^6 $(\mathrm{N \cdot m})/\mathrm{m}$.

The rotation-to-force stiffness ($K_{\theta f}$) depicted in Fig. 13c reveals that shrink-fit holders maintain notably higher values than other holder types, particularly at larger diameters. Finally, Fig. 13d shows the rotation-to-moment stiffness ($K_{\theta m}$), where all holder types exhibit similar exponential behaviour with increasing diameter, though the shrink-fit holder maintains a slight advantage.

Across all four stiffness parameters, the data demonstrates that the influence of diameter reduction is most pronounced in the smaller diameter range (10–12 mm), where the differences between holder types become more significant. The resultant hierarchy of holder stiffness, in descending order, emerged as: shrink-fit, high-power, hydraulic, and collet holders. This behaviour is particularly evident in the rotation-to-force $K_{\theta f}$ parameter, where stiffness values can differ by an order of magnitude between holder types at smaller diameters. These findings provide crucial insights for the selection of holder configurations.

While stiffness parameters show clear trends as demonstrated in Fig. 13, a similar analysis was conducted for damping parameters across the various holder-tool configurations. However, damping parameters exhibited substantially more complex behaviour with non-monotonic relationships that varied significantly between holder types. The damping data showed higher measurement-to-measurement variability

Table 2
Properties of the shrink-fit holder-tool contact dynamics interface.

Holder-tool interface								
Methodology	k_{xf} (N/m)	c_{xf} (N·s/m)	k_{xm} (N·m/m)	c_{xm} (N·s)	$k_{\theta f}$ (N/rad)	$c_{\theta f}$ (N·s/rad)	$k_{\theta m}$ (N·m/rad)	$c_{\theta m}$ (N·m·s/rad)
Proposed	1.97×10^7	53.86	5.7×10^6	99.84	6.86×10^5	27.78	7.73×10^4	0.99
Albertelli	2.23×10^7	52.52	6.93×10^6	62.47	4.35×10^5	18.75	6.49×10^4	1.01
Schmitz	2.60×10^7	59.24	4.62×10^6	103.52	4.33×10^5	19.54	5.98×10^4	1.12

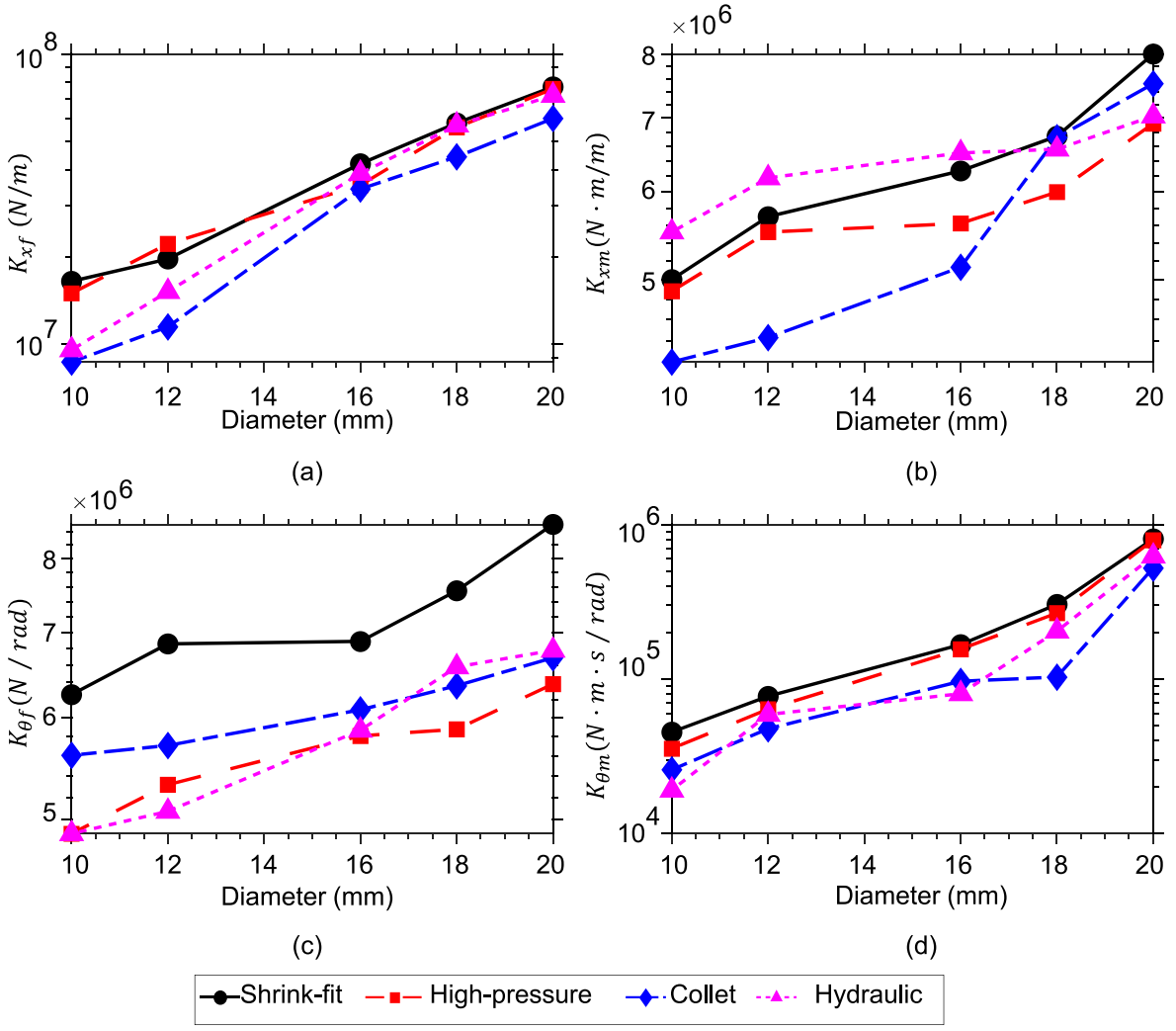

Fig. 13. Effect of diameter on stiffnesses of the holder-tool contact interface. (a) displacement-to-force stiffness, (b) displacement-to-moment stiffness, (c) rotation-to-force stiffness, and (d) rotation-to-moment stiffness.

compared to stiffness parameters and revealed interactions between multiple competing physical mechanisms including micro-slip phenomena, contact pressure distribution variations, and material property interactions at the interface boundaries. This complexity in damping behaviour aligns with observations in previous studies on joint interfaces, where researchers typically focus on stiffness parameters due to their more consistent and predictable nature [11]. The contact interface damping mechanisms involve multiple overlapping physical processes that cannot be simplified into the clear diameter-dependent relationships observed with stiffness. For practical engineering applications, the stiffness parameters presented in Fig. 13 provide more robust and actionable guidance for selecting appropriate holder configurations in industrial settings.

In addition to diameter effects, tool insertion length is another critical parameter affecting contact stiffness. Our testing methodology standardised the insertion length at 40 mm across all holder-tool configurations, as this represents a widely recommended insertion length in industrial applications. However, research by Liao et al. [10] has demonstrated that contact stiffness increases significantly with insertion length. Their findings show that increasing tool insertion length from 26 to 41 mm results in approximately 55 % higher static stiffness and 59 % greater contact force. This suggests that when changing the length of the tool clamped in holder, recalibration of the contact stiffness matrix becomes necessary to maintain prediction accuracy. The effect is particularly important in industrial applications where various tool projection lengths may be required for different machining operations while using the same holder type.

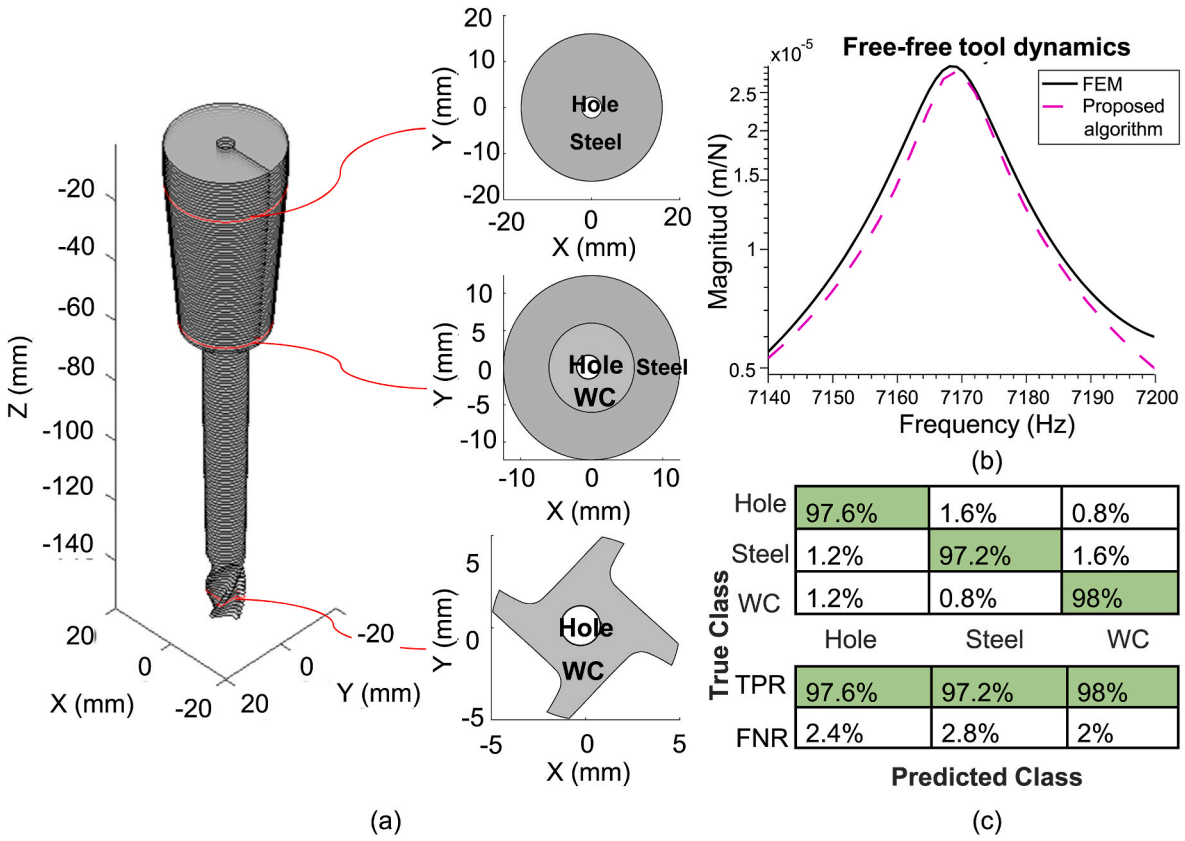

Fig. 14. Slicing-Machine Learning (ML)-Timoshenko Beam Theory (TBT)-Receptance Coupling Substructure Analysis (RCSA) algorithm used to model the cutting tool from Fig. 10c. (a) Slices with the predicted components, (b) comparison of first vibration mode obtained with a FEM model and the proposed algorithm, and (c) confusion matrix of the trained machine learning model.

3.4. Free-free dynamic modelling using a slicing-ML-TBT-RCSA algorithm

The tungsten carbide tool (T2) and steel holder (H2), previously modelled in 3D, were converted into STL format to obtain cross-sections using the slicing algorithm. Fig. 14a displays the slices, which were spaced at 1 mm intervals, and highlights three representative slices where the components and their materials are identified and labelled. The properties of the steel (E = 200 GPa, $\rho = 7800$ kg/m^3, $\upsilon = 0.3$, and $\eta = 0.0015$) and tungsten carbide (E = 585 GPa, $\rho = 14500$ kg/m^3, $\upsilon = 0.21$, and $\eta = 0.0015$) were sourced from previously published research [14]. A geometry-based shear correction factor algorithm was integrated into the model to improve the accuracy of shear deformation analysis using the equations proposed in Ref. [29]. These equations account for the variation of shear stress across different cross-sectional geometries, enhancing the accuracy of the shear deformation modelling. The mixing law was applied to each slice, considering the proportion of the area occupied by each component to determine the resulting properties of the slice. Subsequently, the Timoshenko free-free beam equations derived in Ref. [4] were utilised to obtain the receptance matrix for each slice. Using the RCSA equations [36], these individual slices were then joined to form the full free-free receptance of the cutting tool. The effect of the tool diameter on the contact stiffness matrix of the holder-tool contact interface, as obtained from the analysis in the previous subsection, was incorporated into the receptance coupling process.

The machine learning model for predicting materials based on geometrical features was evaluated for accuracy and reliability using twenty tools in STL format, with varying geometries of carbide bodies tools and steel holders. These holder-tools were sliced, and each component was labelled as body (WC), cooling channel (holes), or holder (steel), creating a balanced dataset with 250 samples per component. Eight geometric features were selected via chi-square analysis: area, x-moment of inertia, y-moment of inertia, xy-moment of inertia, perimeter, mean curvature, aspect ratio, and slice height, and normalised using z-scores. Five machine learning models were tested and optimised, with the support vector machine (SVM) using a Gaussian kernel function, achieving the highest accuracy at 97.6 %. The confusion matrix (Fig. 14c) showed high true positive rates (TPR), with accuracy rates of 97.6 % for holes, 97.2 % for steel, and 98 % for WC. Positive predictive values (PPV) were 98 % for holes, 98.8 % for steel, and 97.3 % for WC, while false discovery rates (FDR) were low at 2 %, 1.2 %, and 2.7 %, respectively. These metrics highlight the accuracy and reliability of the model, crucial for accurately identifying materials and geometrical properties in free-free tool dynamics using Timoshenko beam equations.

The free-free dynamic response of the tool obtained with the slicing-ML-TBT-RCSA algorithm was compared with a simulation of multibody dynamics in COMSOL. The joints between the tool and holder were modelled as prismatic joints with the properties listed in Table 2. A physically controlled sequence with fine-sized elements was used for meshing. This analysis was restricted to the frequency range of 7100–7200 Hz, with increments of 1 Hz, to manage simulation time effectively. The first vibration mode obtained with the FEM model and the proposed algorithm are illustrated in Fig. 14b. It is noteworthy that both the analytical model and the FEM model accurately predicted the first mode of vibration. However, our model required only ~14 s to compute all the receptances at 1 Hz resolution, whereas the FEM analysis took ~380 s for the specified frequency range.

Fig. 15 presents the efficacy of machine learning for automated classification of cutting tool components and its impact on dynamic response prediction accuracy. This study evaluated how different material configurations and identification of internal holes (e.g., cooling

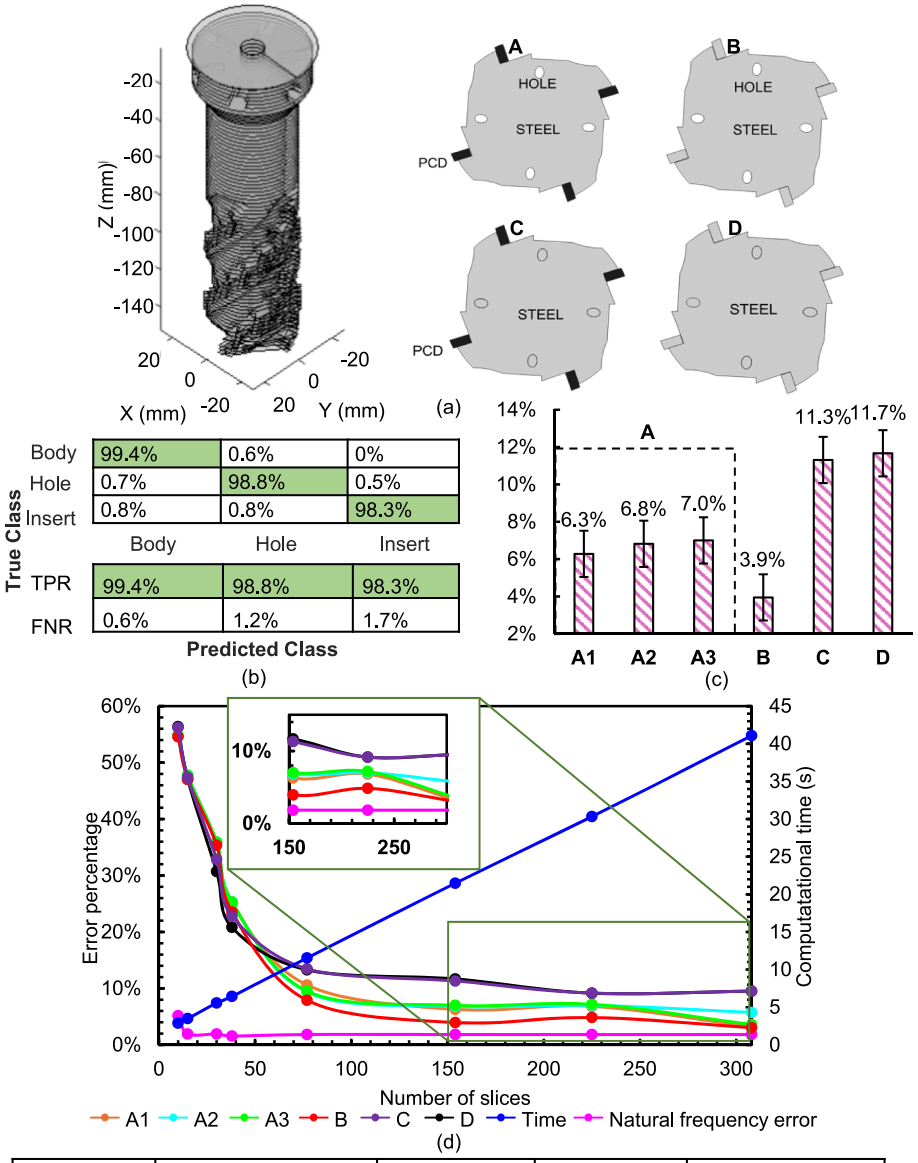

Material	Young's modulus (GPa)	Density(kg/m³)	Poisson's ratio	Solid damping factor
Steel	200	7800	0.3	0.0015
PCD0.85 (A1)	827	4370	0.08	0.0015
PCD10 (A2)	1000	4090	0.1	0.0015
PCD25 (A3)	1100	3790	0.1	0.0015

Fig. 15. Machine learning-based classification of cutting tool components and analysis of material influence on dynamic response accuracy. (a) 3D sliced representation of a stepped helical monoblock tool with cross-sections showing material distribution of steel, Polycrystalline Diamond (PCD) inserts, and holes. (b) Confusion matrix showing classification accuracy for body, hole, and insert, (c) Material contribution to predicted dynamic response accuracy at 150 slices, (d) Resolution analysis showing relationship between slice count and prediction error with computational time overlay.

channels) affect frequency response function predictions for the S-T5 stepped helical monoblock tool with brazed PCD inserts. The investigation utilised the proposed sliced 3D tool model with supervised learning to classify components (body, holes, inserts) and assign appropriate material properties. Tests were conducted across multiple configurations with varying PCD material properties according to grain size (0.85 μm, 10 μm, and 25 μm) to determine factors influencing dynamic response accuracy. All prediction errors were compared against tool tip dynamics obtained by tap-testing after the tool was clamped to the machine using the proposed method (Fig. 12).

The machine learning model for predicting materials based on geometrical features was evaluated for accuracy and reliability using ten tools in STL format with varying geometries. These tools were sliced, and each component was labelled as body, hole, or insert, creating a balanced dataset with 300 samples per component. Eight geometric features were selected via chi-square analysis: area, x-moment of inertia, y-moment of inertia, xy-moment of inertia, perimeter, mean curvature, aspect ratio, and slice height, and normalised using z-scores. Five machine learning models were tested and optimised, with the support vector machine (SVM) using a Gaussian kernel function achieving the highest accuracy. The confusion matrix (Fig. 15b) showed exceptionally high true positive rates (TPR), with accuracy rates of 99.4 % for body, 98.8 % for hole, and 98.3 % for insert components. The corresponding false negative rates (FNR) were remarkably low at 0.6 %, 1.2 %, and 1.7 %, respectively.

In panel (C), the configurations A1, A2, and A3 show error rates of

6.3 %, 6.8 %, and 7.0 % corresponding to PCD materials with different grain sizes. These variations demonstrate model sensitivity to material properties, yet their limited impact must be contextualised. PCD inserts, though critical for cutting performance, constitute a relatively small portion of the total tool volume, thus their influence on dynamic behaviour remains constrained. This explains why substantial variations in PCD properties with Young's modulus from 827 GPa to 1100 GPa produced only marginal changes in prediction error. Configuration B shows superior performance (3.9 % error) with conventional materials and internal geometries without PCD components. Conversely, configurations C and D exhibit higher errors (11.3 % and 11.7 %), highlighting the importance of accurate material and void identification for reliable predictions.

Panel (d) reveals a critical relationship between geometric resolution and prediction accuracy. Error percentages decrease dramatically as the number of slices increases from 0 to approximately 50 (requiring about 8 s of computation), demonstrating the fundamental importance of geometric fidelity for the complex stepped helical structure. Beyond 150 slices (approximately 25 s of computational time), the error reduction diminishes substantially for all configurations while computational time continues to increase linearly, reaching about 40 s at 300 slices. This indicates an optimal operational range of 150-200 slices that balances accurate geometric representation with computational efficiency. The zoomed-in view confirms that natural frequency error stabilises below 1 % once sufficient geometric resolution is achieved, regardless of material configuration variations.

The accurate geometric modelling achieved by the algorithm explains why the prediction errors remain within acceptable ranges despite material variations. The consistent identification of steel as the major component (with 99.4 % accuracy) contributes significantly to model stability, as steel constitutes the largest fraction of the monoblock tool body. This dominant material consistency, combined with accurate void detection, explains why the reported errors remain well within the amplitude measurement variability of 10.23 % relative to the mean. Most notably, the accurate modelling of structural geometry and primary material enables natural frequency prediction errors to remain consistently below 0.88 %, confirming excellent accuracy regardless of secondary material configurations.

These findings establish that while secondary material property assignment contributes to prediction quality, the capability to identify internal holes and consistently classify the primary steel structure represents the most valuable advancement for practical cutting tool dynamic analysis. The relationship between slice resolution and prediction accuracy confirms that geometric fidelity is the dominant factor in achieving reliable dynamic predictions, enabling accurate characterisation without requiring destructive testing or specialised imaging techniques.

3.5. *Predictive capability assessment of tool tip dynamics*

The machine-spindle-flange receptance matrix $[G_{55}]$ and the free-free dynamics of the holder-tool determined in the previous subsections were coupled using RCSA to predict the tool tip dynamics. The critical vibration modes obtained by tap-testing and predicted by the proposed methodology and previous studies is shown in Fig. 16. The tool free-free FRFs were obtained consistently across all three methods using our slicing-ML-TBT-RCSA algorithm to ensure fair comparison. The proposed methodology achieved significantly lower natural frequency errors of 0.40 % for the first mode and 0.08 % for the second mode, compared to Albertelli et al. (4.73 % and 1.11 %) and Schmitz et al. (4.73 % and 1.51 %). Additionally, the Schmitz et al. method generated an extra non-physical mode at 1529 Hz, which was not observed experimentally by tap-testing. Amplitude errors from the proposed methodology were limited to 0.40 % and 2.40 % for the first and second modes, respectively, while Albertelli et al. exhibited substantially larger errors of 28.14 % and 21.09 %, and Schmitz et al. showed errors of 5.39 % and 43.03 %. These findings confirm the enhanced accuracy of the proposed methodology in predicting tool tip dynamics, avoiding extra modes and significantly improving predictive accuracy.

Figs. 17 and 18 show the FRFs of the holder-tool configurations depicted in Fig. 11, comparing tap-testing measurements with predictions from the proposed methodology. Across all evaluated

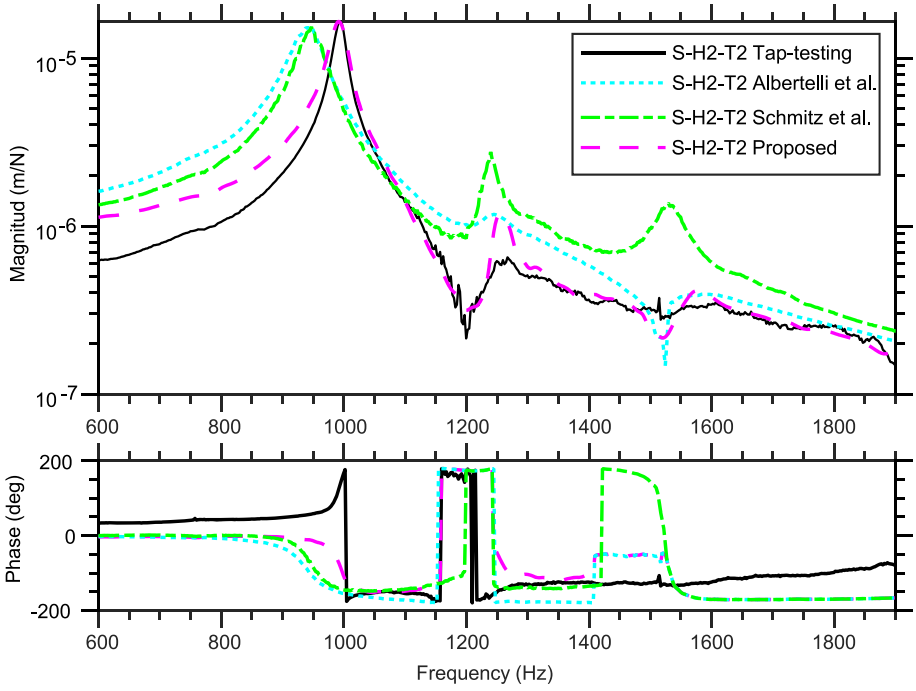

Fig. 16. Comparison of tool tip dynamic response predicted by different Receptance Coupling Substructure Analysis (RCSA) methodologies and validated through experimental tap-testing. The Frequency Response Functions (FRFs) for the Holder 2–Tool 2 (H2-T2) configuration are compared across the proposed approach, methods by Albertelli et al. and Schmitz et al., and tap-testing.

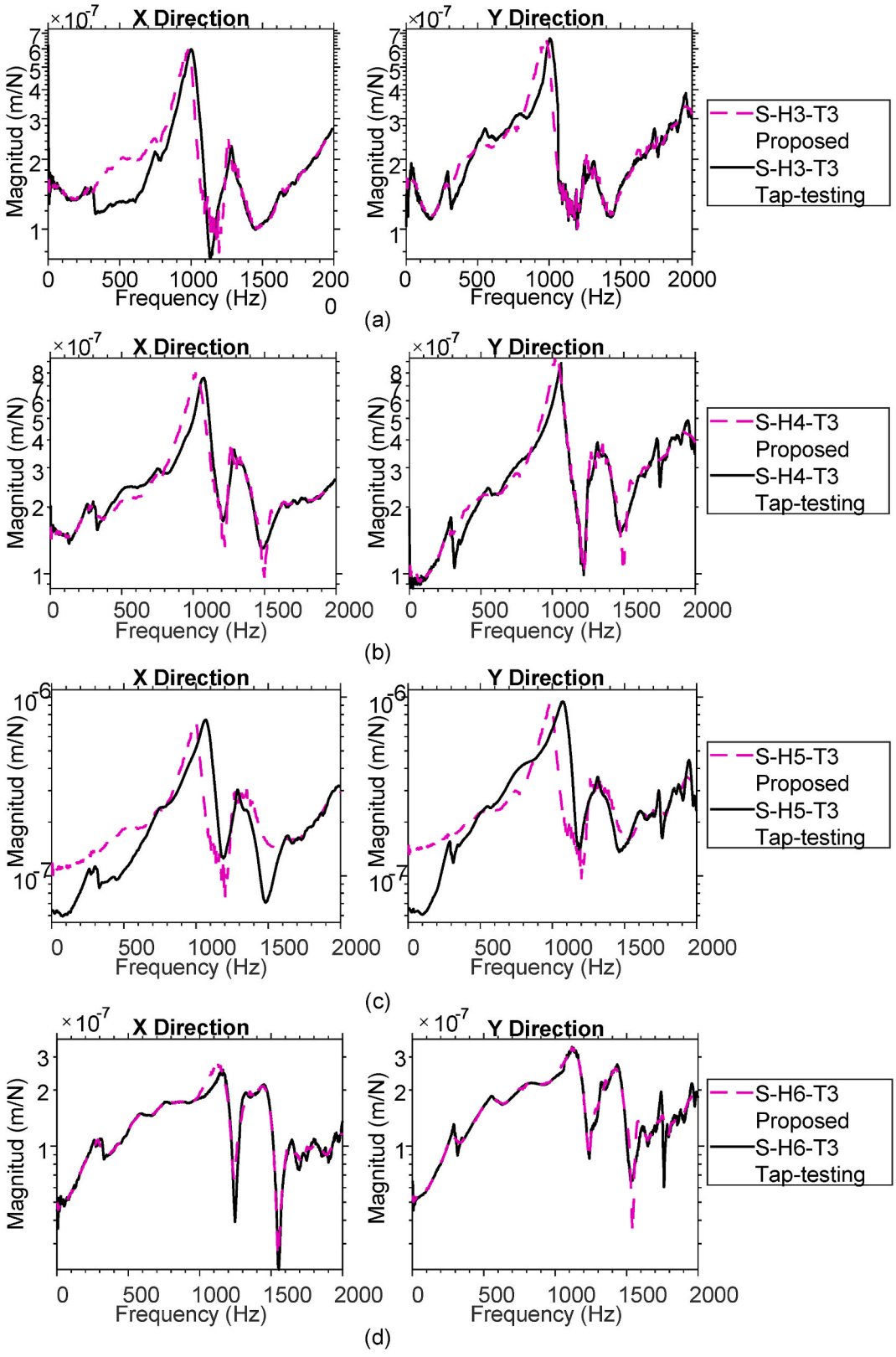

Fig. 17. Comparison of Frequency Response Functions (FRFs) obtained using the proposed methodology and experimental tap-testing across different holder configurations. (a) Spindle with Holder 3 and Tool 3 (S-H3-T3), (b) Spindle with Holder 4 and Tool 3 (S-H4-T3), (c) Spindle with Holder 5 and Tool 3 (S-H5-T3), (d) Spindle with Holder 6 and Tool 3 (S-H6-T3).

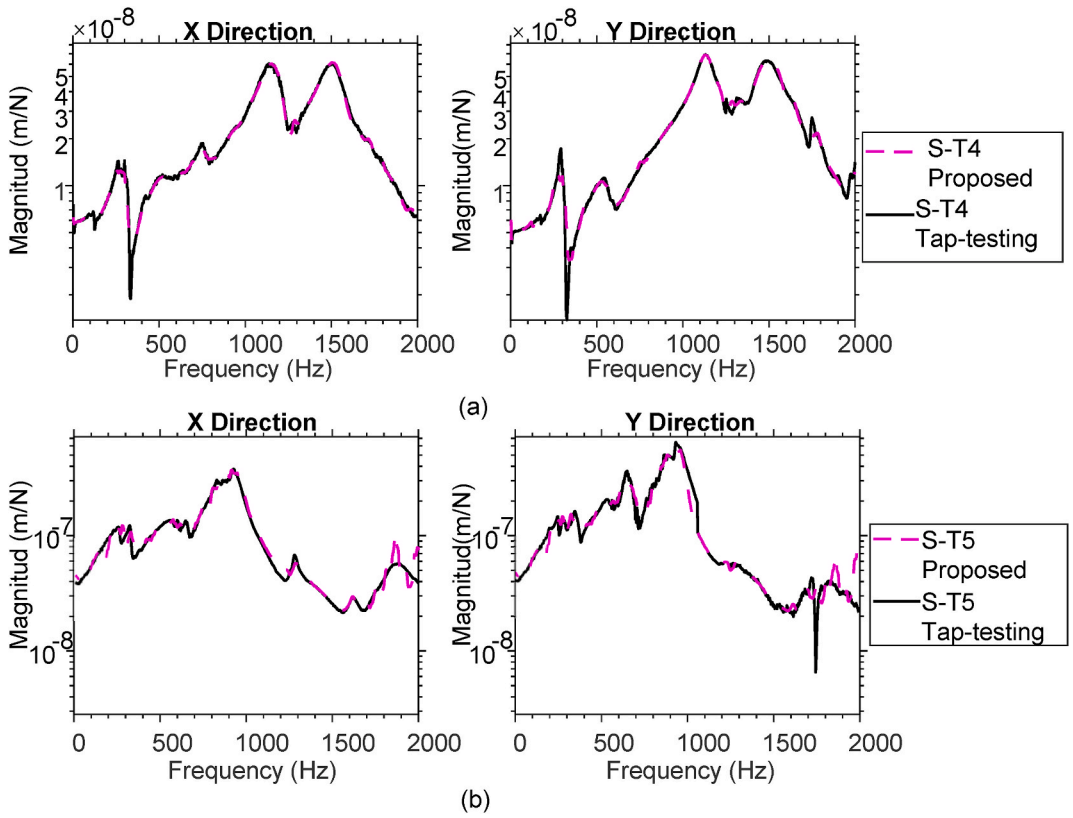

Fig. 18. Comparison of Frequency Response Functions (FRFs) obtained using the proposed methodology and experimental tap-testing for asymmetric, non-slender tool configurations. (a) Spindle with Tool 4 (S-T4), (b) Spindle with Tool 5 (S-T5).

configurations, the methodology demonstrates robust predictive performance. In the critical modes, frequency predictions achieve an average accuracy of 2.2 % (spanning 0.2 %–4.7 %), and amplitude predictions maintain an average accuracy of 4.1 % (ranging 2.2 %–7.9 %).

3.6. Chatter-free machining validation

The stability lobe diagrams (SLDs) were generated to evaluate and compare different methods for predicting tool tip dynamics in machining operations. The experimental results, obtained by tap-testing, served as a benchmark for assessing three prediction methods: Albertelli et al., Schmitz et al., and our proposed methodology (Fig. 19). The comparison revealed that our proposed method achieved closer alignment with the tap-testing results, particularly at higher spindle speeds (above 13000 rpm), where the critical depth of cut reached its maximum value of approximately 3 mm at 14900 rpm.

The validation of these methods was further substantiated through practical machining tests, represented by green circles (stable) and red crosses (unstable) in the diagram. The tabulated results in Fig. 19c provide additional evidence of the reliability of our methodology, demonstrating the relationship between radial depth of cut (a_e) and surface quality for various axial depths of cut (a_p). These observations were further confirmed by frequency spectra obtained from accelerometer measurements mounted on the machining head, comparing axial depths of cut of 3 mm (stable) and 4 mm (unstable). Prominent chatter frequencies were distinctly present only under the unstable machining condition. Nonetheless, at spindle speeds close to resonance, such as 14,900 rpm, chatter frequencies began to emerge at lower amplitudes even under stable conditions (3 mm), although these were insufficient to produce visible chatter marks on the machined surfaces.

The SLDs in Fig. 20 demonstrate robust agreement between predicted and experimental results across all the four holder-tool configurations. Additionally, the machining trials, denoted by green circles for stable conditions and red crosses for unstable conditions, provide compelling evidence of the reliability of the method over a wide range of machining conditions (3000–19,000 rpm). Notably, the theoretical model successfully predicts the characteristic peaks at 8000 and 16000 rpm in configuration S-H3-T3, the intermediate stability regions at 4–5 mm depth in S-H4-T3, the transitions from stable to unstable conditions, and the complex multi-lobe patterns in S-H6-T3.

Comparative analysis of the holder configurations reveals that the S-H3-T3 setup (Fig. 20a) demonstrates superior characteristics for maximising material removal rates, exhibiting stable cutting depths of up to 6 mm at the best spindle speed of 9400 rpm. This superior performance can be attributed to the robustness of the shrink-fit holder (shorter overhang of 54 mm compared to 79, 73, and 67 mm of the other holders) and the higher contact dynamics stiffness values, as determined in the contact stiffness matrix analysis (Fig. 13). In contrast, the S-H4-T3 and S-H5-T3 configurations display progressively reduced stability limits, with maximum stable cutting depths of 4–5 mm and 4 mm, respectively, whilst the S-H6-T3 holder exhibits the most conservative stable cutting depths of 2–3 mm.

The notably close correlation between predicted and experimental stability boundaries warrants further discussion. Several factors might explain this agreement. Firstly, the tested configurations appear to have dominant compliance in the holder-tool assembly rather than the spindle, as evidenced by the modal parameters in Table 3. This suggests that spindle-borne variations due to rotation, thermal expansion, and changes in bearing preload have a minimal influence on the critical modes governing stability. Secondly, the testing was conducted within the operational speed range of 3000–19,000 rpm, which falls within the stable working range of the GF P800 U machine tool. The GF P800 U features a robust bearing system that maintains consistent dynamic characteristics throughout these testing conditions, contributing to the stability of the measurements. Additionally, the careful characterisation

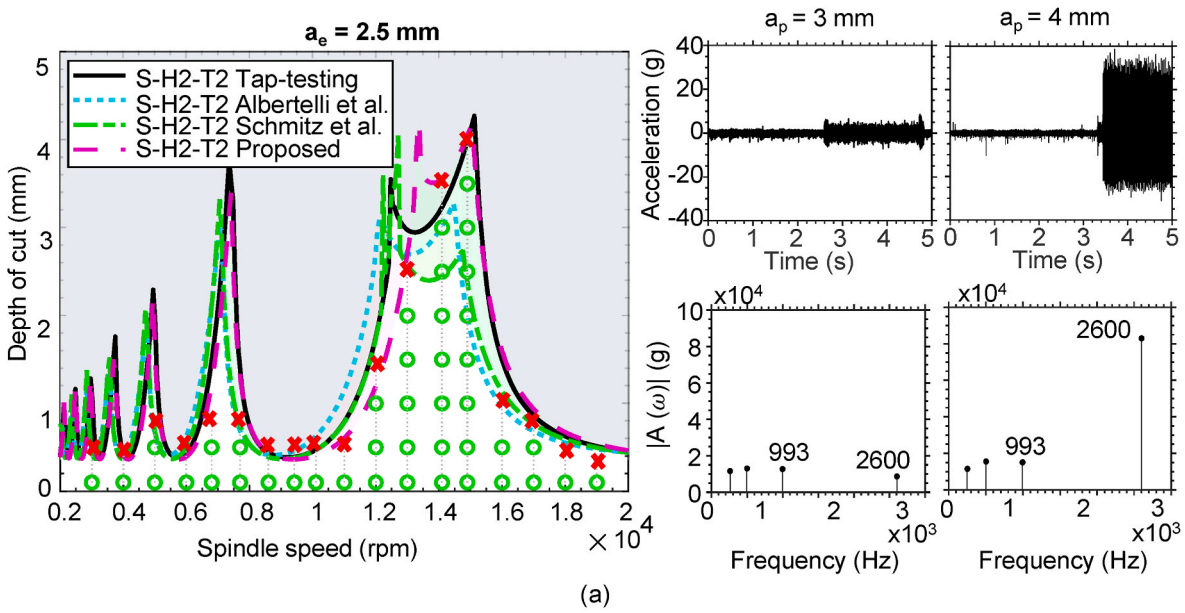

(a)

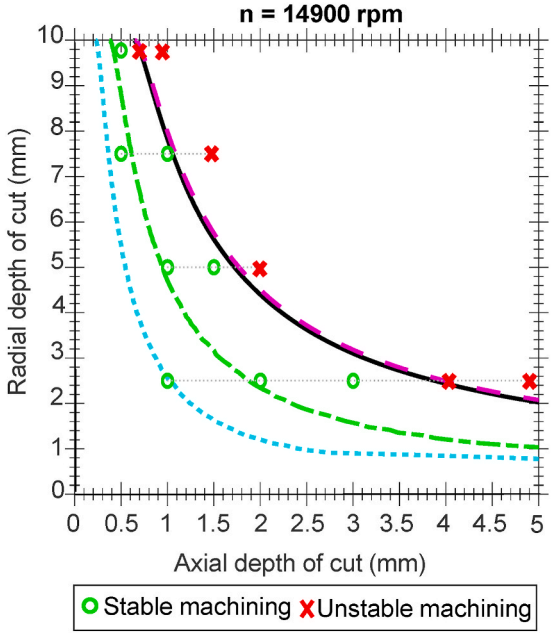

(b)

a_e (mm)	a_p (mm)	Chatter	Surface quality
2.5	3	No	
	4	Yes	
5	1.5	No	
	2	Yes	
7.5	1	No	
	1.5	Yes	
10	0.5	No	
	1	Yes	10 mm

(c)

Fig. 19. Stability analysis and experimental validation of milling tests on A356 aluminium. (a) Stability lobe diagram (SLD) for a radial depth of cut (a_e) of 2.5 mm. Predictions from the proposed and existing methodologies are compared against tap-testing. Right: Time-domain acceleration signals and frequency spectra at 14,900 rpm showing stable (3 mm) to unstable (4 mm) transition, (b) Axial depth of cut (a_p) versus radial depth of cut (a_e) at a constant spindle speed of 14,900 rpm, (c) Surface quality assessment and chatter detection for various cutting conditions. The table summarises the cutting parameters, tangential specific cutting force (K_{tc}), and radial specific cutting force (K_{rc}) used to generate the SLDs.

of contact stiffness matrices across different holder types, as presented in Fig. 13, further enhanced prediction accuracy by capturing the most significant interface dynamics affecting the overall system behaviour.

$$a_{p,lim,power} = \left(P_{lim} \cdot 60x10^6\right) \; / \; \left(k_s \cdot a_e \cdot n \cdot f_z \cdot z\right) \tag{64}$$

The shell-end mill (S-T4) and monoblock tool (S-T5), both featuring larger diameters of 48 mm and 40 mm respectively, introduce different limiting factors. For the S-T4 (Fig. 20e), the substantially larger diameter results in higher power consumption during cutting operations, making machine power limitations more critical than chatter stability. The power limit (blue curve) was approximated using Eq. (64) based on the established cutting conditions. Additionally, the maximum height of the insert constrains the operational envelope at higher removal rates. Similarly, for the S-T5 (Fig. 20f), testing was confined to the second lobe region due to the power constraints associated with its larger diameter, yet still demonstrates excellent correlation between predicted and measured stability boundaries within this operational window.

4. Conclusions and future lines

Despite advances, a comprehensive, cost-effective, and accurate Receptance Coupling Substructure Analysis (RCSA) framework suitable for a production environment has not yet been developed. This paper, therefore, presents a novel computational approach using RCSA that

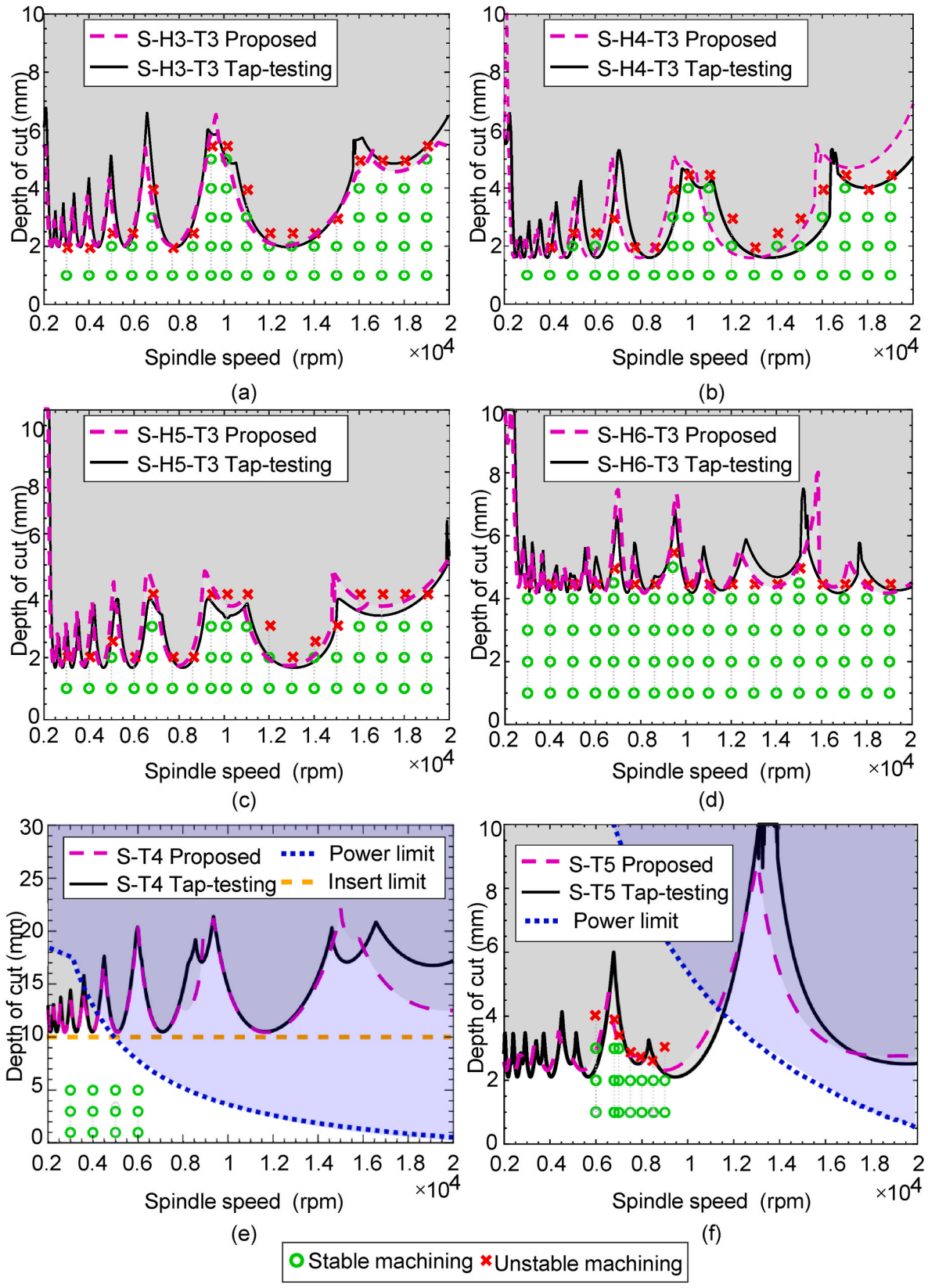

Fig. 20. Comparison of Stability Lobe Diagrams (SLDs) obtained using the proposed methodology and experimental tap-testing for different holder configurations. (a) Spindle with Holder 3 and Tool 3 (S-H3-T3), (b) Spindle with Holder 4 and Tool 3 (S-H4-T3), (c) Spindle with Holder 5 and Tool 3 (S-H5-T3), (d) Spindle with Holder 6 and Tool 3 (S-H6-T3), (e) Spindle with Tool 4 (S-T4), (f) Spindle with Tool 5 (S-T5). The table summarises the cutting parameters, tangential specific cutting force (K_{tc}), and radial specific cutting force (K_{rc}) used to generate the SLDs.

Table 3
Modal parameters obtained from predicted Frequency Response Functions (FRFs) of each holder-tool configuration presented in Figs. 17 and 18.

Mode	1	2	3	4	5	6
S-H3-T3						
ω_n **(rad/s)**	286	555	812	980	1262	1951
ζ (%)	24.3	13.3	11.4	5.6	5.0	5.0
k **(N/μm)**	13.1	16.3	15.5	14.1	47.9	29.5
p_x	0.7	0	0	0.67	0.76	0.59
p_y	0.72	1	1	0.74	0.65	0.81
A **(μm/N)**	0.16	0.23	0.28	0.63	0.21	0.34
Relative error ω_n (%)	2.95	−0.18	0.00	2.23	0.71	0.56
Relative error A (%)	0.34	14.69	−2.25	3.45	0.93	−36.04
S-H4-T3						
ω_n **(rad/s)**	524.79	762.2	1028.59	1307.84	1704.66	1914
ζ (%)	9.05	3.77	5.31	9.78	4.06	2.5
k **(N/μm)**	2.42	4.74	1.08	2.27	5.03	4.61
p_x	0	1	0.65	0.71	0.53	0
p_y	1	0	0.76	0.71	0.78	1
A **(μm/N)**	2.28	2.80	8.72	2.25	2.45	4.34
Relative error ω_n (%)	4.55	0.00	4.68	0.69	1.92	1.68
Relative error A (%)	6.07	0.17	−2.89	18.29	18.40	11.60
S-H5-T3						
ω_n **(rad/s)**	290	1046	1307	1629	1712	1941
ζ (%)	12.9	4.9	10.6	3.5	1.8	1.3
k **(N/μm)**	3.7	1.2	1.4	8.0	11.7	12.1
p_x	0.63	0.61	0.65	0.59	0	0.64
p_y	0.78	0.8	0.76	0.81	1	0.77
A **(μm/N)**	1.06	8.21	3.31	1.79	2.44	3.20
Relative error ω_n (%)	1.19	2.26	−0.20	−1.06	1.44	−0.51
Relative error A (%)	17.51	2.24	5.44	22.32	19.36	5.29
S-H6-T3						
ω_n **(rad/s)**	592	824	1117	1352	1431	1770
ζ (%)	17	13.6	7.9	1.2	4.7	1.7
k **(N/μm)**	17.9	24.3	20.3	228	39.5	120
p_x	0.63	0.62	0.63	0.66	0.63	0.58
p_y	0.77	0.79	0.77	0.75	0.78	0.81
A **(μm/N)**	0.16	0.15	0.31	0.18	0.27	0.25
Relative error ω_n (%)	−3.68	−1.73	2.95	−2.19	0.63	2.80
Relative error A (%)	1.59	−16.50	−2.66	6.69	−10.05	−98.68
S-T4						
ω_n **(rad/s)**	527	697	1132	1155	1504	1774
ζ (%)	15.9	10.6	5.3	5.7	5.2	2.2
k **(N/μm)**	296	334	136	144	155	1050
p_x	0.7	0	0.9	0	1	0
p_y	0.7	1	0.5	1	0	1
A **(μm/N)**	0.01	0.01	0.07	0.06	0.06	0.02
Relative error ω_n (%)	2.76	0.84	0.17	21.96	0	−1.43
Relative error A (%)	5.38	−2.48	−7.92	4.17	−2.95	19.45
S-T5						
ω_n **(rad/s)**	280	327	648	912	827	1279
ζ (%)	17.17	13.86	9.56	7.81	4.80	2.64
k **(N/μm)**	22.2	29.1	22.4	17.1	40.2	278.0
p_x	0.62	0.57	0.41	0	1	1
p_y	0.78	0.82	0.91	1	0	0
A **(μm/N)**	0.13	0.12	0.23	0.37	0.26	0.07
Relative error ω_n (%)	−10.03	7.09	−19.24	2.67	0	0
Relative error A (%)	2.86	24.71	−50.23	42.84	0	0

overcomes the limitations of previous approaches, offering a more efficient and accurate prediction of tool tip dynamics. The proposed computational approach simplifies the estimation of the full receptance matrix by reducing the necessary impact tests to three, using just one accelerometer, and eliminating issues related to extra modes, signal distortion, and additional post-processing.

In this computational approach, estimation of rotational effects is addressed through a dual approach combining rigorous theoretical analysis with practical implementation guidelines. Our mathematical error analysis fundamentally challenges conventional numerical wisdom by demonstrating that first-order finite difference methods should be preferred over second-order methods in specific practical scenarios. Specifically, first-order Finite Difference Approximation (FDA) outperforms second-order approaches when measurement standard deviation exceeds 2.47 % of the mode shape norm for displacement-to-moment (L) and rotation-to-force (N) receptances, and merely 0.47 % for rotation-to-moment (P) receptance calculations. In practical machine tool testing, these thresholds are frequently exceeded due to sensor placement errors, impact force variations, and environmental factors. Given that the P receptance is particularly sensitive to measurement errors due to its calculation requiring mixed spatial derivatives, the advantage of first-order methods becomes especially pronounced for this crucial component of tool tip dynamics prediction.

Building upon this theoretical foundation, we provide practical guidelines for selecting a suitable measurement spacing (s) in the FDA approach through analytical error analysis and s-selection maps. These maps play a crucial role in determining the optimal s value, given the length and diameter of the holder and tool, to accurately calculate the full machine-spindle receptance matrix and the contact stiffness matrix.

The methodology also incorporates a time-efficient and accurate free-free tool dynamics modelling approach. This is achieved by integrating an enhanced Stereolithography (STL) slicing algorithm and machine learning techniques with Timoshenko beam theory and RCSA. The automated approach uniquely identifies tool components and material transitions directly from STL files. This enables accurate prediction of dynamic behaviour for complex cutting tools with variable cross-sections, multiple inserts, and internal cooling channels. Unlike previous methodologies [15,16], which require additional Finite Element Analysis (FEA) software, this approach can be entirely developed within a unified algorithm. As a result, the proposed methodology is more accessible and easier to implement in an industrial setting.

The proposed computational approach using RCSA offers a streamlined, accurate, and industrially applicable method for predicting tool tip dynamics. It predicts the vibration mode at the same frequency, with an error of 2.2 %, and generates predicted Stability Lobe Diagrams (SLDs) in about 20 s. Employing this computational approach, manufacturers can select suitable cutting parameters and design cutting tools to increase material removal rate and reduce cycle times, thereby maximising return on investment (ROI).

Future research could focus on two primary directions. Firstly, future work could validate this computational approach across a broader range of machining scenarios, which might include integrating the workpiece fixturing system into the framework using RCSA. Research could also conduct a sensitivity analysis to examine the effects of variations in machines of the same reference/manufacturer, changes in spindle performance over time, machine-spindle overhang, and machining

positioning would also be of value to industry. Secondly, while our computational approach demonstrates significant practical advantages in terms of efficiency and accuracy, a key limitation is that it does not deeply explore the underlying physical mechanisms at tool-holder interfaces. Future work should address this limitation by investigating non-linear contact mechanics, micro-slip behaviour at interfaces, and energy dissipation processes. This deeper physical understanding would complement the practical approach developed in this study and potentially lead to further improvements in prediction accuracy.

CRediT authorship contribution statement

Jesus David Chaux: Writing – review & editing, Writing – original draft, Visualization, Validation, Software, Methodology, Investigation, Formal analysis, Data curation, Conceptualization. **Patxi X. Aristimuño Osoro:** Writing – review & editing, Supervision, Methodology, Funding acquisition, Formal analysis, Conceptualization. **Pedro J. Arrazola:** Writing – review & editing, Supervision, Resources, Project administration, Funding acquisition, Conceptualization.

Declaration of competing interest

The authors declare that they have no known competing financial interests or personal relationships that could have appeared to influence the work reported in this paper.

Acknowledgements

The authors hereby thank the DIGIVaCh (ZE-2021/00026), TAILORSURF (PID2022-139655OB-I00) and ORLEGI (KK-2024/00013) projects for their financial support.

Appendix A. Derivation of the Full Receptance Matrix Components Using Finite Difference Approximations

This appendix presents the mathematical formulations for finite difference approximations (FDA) required for rotational degree-of-freedom synthesis and the derivation of the full receptance matrix components.

A.1 Derivation of the Full Receptance Matrix Components Using Finite Difference Approximations

A.1.1 Rotation-to-Force Receptance

The displacement is measured successively at each point of a set of points adjacent to point j with the excitation held at point i. The instantaneous angular displacement of the structure at a location relative to its rest position is given by

$$\theta = \frac{dW}{dx_1} \tag{65}$$

$$\theta(\omega, x_1) = \frac{d}{dx_1} W(\omega; x_1) \tag{66}$$

From which is formed the ratio of complex amplitudes

$$\frac{\theta_j(\omega)}{F_i(\omega)} = \frac{d}{dx_1} \frac{W(\omega; x_1)}{F_i(\omega)} \tag{67}$$

To obtain in terms of receptance

$$H_{\theta_j F_i} = \frac{d}{dx_1} H_{WF_i}(\omega; x_1) \tag{68}$$

Assuming that H is dependent only on the x_1 coordinate space, the continuous derivative can be approximated by the FDA. First and second order derivatives are obtained by

$$\frac{dH_{x_1,x_2}}{dx_1} = \frac{H_{x_1,x_2} - H_{x_1-s_1,x_2}}{s_1} + O(s_1^1) \tag{69}$$

$$\frac{dH_{x_1,x_2}}{dx_1} = \frac{3H_{x_1,x_2} - 4H_{x_1-s_1,x_2} + H_{x_1-2s_1,x_2}}{2s_1} + O(s_1^2) \tag{70}$$

Where the subscript x_1 corresponds with the position of the accelerometer spaced s_1 apart, subscript x_2 with the location of the impact hammer hit, and $O(s_1^p)$ represents the p-order dependent error function in the FDA. The backward FDA is employed, as we are particularly interested in calculating the derivative at the tool tip.

A.1.2 Displacement-to-Moment Receptance

The excitation force is applied at each point of a set of points adjacent to point i with the responses measured at point j. An instantaneous moment applied to the structure at Point i could be equivalently represented as a pair of equal and opposite parallel forces separated by a small distance, ϵ. The response of the structure at point j would be

$$W_j(\omega) = \lim_{\epsilon \to 0} \left(W_j(\omega) F(\omega; x_2)|_{x_2 = X_i + \epsilon} - W_j(\omega) F(\omega; x_2)|_{x_2 = X_i} \right) F(\omega) \tag{71}$$

$$W_j(\omega) = \frac{d}{dx_2} \frac{W_j(\omega)}{F(\omega; x_2)}|_{x_2 = X_i} M_i(\omega) \tag{72}$$

From which is formed the ratio of complex amplitudes

$$\frac{W_j(\omega)}{M_i(\omega)} = \frac{d}{dx_2}\frac{W_j(\omega)}{F(\omega;x_2)}\Big|_{x_2=X_i} \tag{73}$$

To obtain in terms of receptance

$$H_{W_jM_i} = \frac{d}{dx_2}H_{W_jF_i}(\omega;x_2) \tag{74}$$

As in rotation-to-force derivation, first and second order derivatives could be obtained using FDA

$$\frac{dH_{x_1,x_2}}{dx_2} = \frac{H_{x_1,x_2} - H_{x_1,x_2-s_2}}{s_2} + O(s_2^1) \tag{75}$$

$$\frac{dH_{x_1,x_2}}{dx_2} = \frac{3H_{x_1,x_2} - 4H_{x_1,x_2-s_2} + H_{x_1,x_2-2s_2}}{2s_2} + O(s_2^2) \tag{76}$$

It is of interest to note that the terms of the rotation-to-force and displacement-to-moment receptances could be assumed to be equal using the Maxwell-Betti reciprocal work theorem (or principle of reciprocity)

$$\frac{dH_{x_1,x_2}}{dx_1} = \frac{dH_{x_1,x_2}}{dx_2} \tag{77}$$

$$H_{\theta_jF_i} = H_{W_jM_i} \tag{78}$$

A.1.3 Rotation-to-Moment Receptance

If the location coordinate x_2 of the force application point is made to vary about X_i, the resultant derivative of translational mobility relates the complex amplitude of translational velocity at Point j to the complex amplitude of applied moment at Point i

$$\frac{\theta_j}{M_i} = \frac{\partial}{\partial x_1}\frac{\partial}{\partial x_2}\frac{W(\omega,x_1)}{F(\omega,x_2)}\Big|_{x_1=X_j,x_2=X_i} \tag{79}$$

To obtain in terms of receptance

$$H_{\theta_jM_i} = \frac{\partial^2}{\partial x_1 \partial x_2}H_{WF}(\omega;x_1;x_2) \tag{80}$$

A.1.4 Full Receptance Matrix Summary

According to the above equations, each element of the full receptance matrix can be expressed in terms of $H_{W_jF_i}$

$$\begin{pmatrix} w_j \\ \theta_j \end{pmatrix} = \begin{bmatrix} H_{W_jF_i} & \frac{\partial}{\partial x_2}H_{W_jF_i} \\ \frac{\partial}{\partial x_1}H_{W_jF_i} & \frac{\partial^2}{\partial x_1 \partial x_2}H_{W_jF_i} \end{bmatrix} \begin{pmatrix} F_i \\ M_i \end{pmatrix} \tag{81}$$

For practical experimental purposes, $s_1 = s_2 = s$. The full receptance matrix at the tool tip occurs when $i = j = 1$

$$\begin{pmatrix} w_1 \\ \theta_1 \end{pmatrix} = \begin{bmatrix} H_{1,1} & L_{1,1} \\ N_{1,1} & P_{1,1} \end{bmatrix} \begin{pmatrix} F_1 \\ M_1 \end{pmatrix} \tag{82}$$

A.2 Univariate Finite Difference Approximations

Given a small spacing value $s > 0$, the derivative of order m for a univariate function $\varphi_r(x)$ can be approximated

$$\phi_r^{(m)}(x) = \frac{m!}{s^m}\sum_{i=i_{min}}^{i_{max}} C_i\phi_r(x+is) + O(s^p) \tag{83}$$

where $p > 0$ represents the order of accuracy of the approximation, and the extreme indices i_{min} and i_{max} are chosen subject to the constraints $i_{max} - i_{min} + 1 = m + p$. The coefficients C_i are determined from Taylor series expansions to achieve the desired accuracy.

A forward-difference approximation occurs when $i_{min} \geq 0$, a backward-difference approximation when $i_{max} \leq 0$, and a central-difference approximation when $i_{min} < 0 < i_{max}$ with $i_{max} = -i_{min}$

A.3 Bivariate Finite Difference Approximations

For bivariate functions, given small spacing values $s_1 > 0$ and $s_2 > 0$, the mixed partial derivative of orders m_1 and m_2 can be approximated as

$$\phi_r^{(m_1,m_2)}(x_1,x_2)=\left(\frac{m_1!}{s_1^{m_1}}\frac{m_2!}{s_2^{m_2}}\right)\sum_{i_1=i_{1,min}}^{i_{1,max}}\sum_{i_2=i_{2,min}}^{i_{2,max}}C_{i_1,i_2}\phi_r(x_1+i_1s_1,x_2+i_2s_2)+\max_{1\le j\le 2}\left\{O\left(s_j^{p_j}\right)\right\} \tag{84}$$

The coefficients C_{i_1,i_2} are obtained as the outer product of the univariate coefficients $C_1=\left(C_{1,i_1,min},\ldots,C_{1,i_1,max}\right)$ and $C_2=\left(C_{2,i_2,min},\ldots,C_{2,i_2,max}\right)$. The j index corresponds to x_j.

A.4 Error Analysis Parameters

The total error in a finite difference approximation arises from two sources.

1. Truncation error, which depends on the order of the approximation and is proportional to s^n
2. Propagation error, which amplifies measurement noise and is inversely proportional to s^m

For the error analysis presented in Section 2.2, the optimum spacing is derived as

$$s_{min}=\left(\frac{m\cdot m!\cdot M_r\sum_{i=i_{min}}^{i_{max}}\left|C_i\right|}{nT\parallel\phi_r^{(n+1)}\parallel}\right)^{\frac{1}{n+m}} \tag{85}$$

where M_r is the measurement perturbation bound, n is the order of the finite difference scheme, and T is the truncation coefficient.

A.5 Tables of Finite Difference Formulae

Table A.1
Finite difference formula for first-order derivatives ($n=1$)

Method	Formula	Order of Accuracy (p)	$\sum\lvert C_i\rvert$	T
Backward	$\frac{\phi_r(x)-\phi_r(x-s)}{s}$	$O(s)$	2	1/2
Forward	$\frac{\phi_r(x+s)-\phi_r(x)}{s}$	$O(s)$	2	1/2
Central	$\frac{\phi_r(x+s)-\phi_r(x-s)}{2s}$	$O(s^2)$	1	1/6

Table A.2
Finite difference formula for second-order derivatives ($n=2$)

Method	Formula	Order of Accuracy (p)	$\sum\lvert C_i\rvert$	T
Backward	$\frac{3\phi_r(x)-4\phi_r(x-s)+\phi_r(x-2s)}{2s}$	$O(s^2)$	4	1/3
Forward	$\frac{-3\phi_r(x)+4\phi_r(x+s)-\phi_r(x+2s)}{2s}$	$O(s^2)$	4	1/3
Central	$\frac{-\phi_r(x+2s)+8\phi_r(x+s)-8\phi_r(x-s)+\phi_r(x-2s)}{12s}$	$O(s^4)$	3/2	1/30

Table A.3
Finite difference formulae for third-order derivatives ($n=3$)

Method	Formula	Order of Accuracy (p)	$\sum\lvert C_i\rvert$	T
Backward	$\frac{11\phi_r(x)-18\phi_r(x-s)+9\phi_r(x-2s)-2\phi_r(x-3s)}{6s}$	$O(s^3)$	20/3	1/4
Forward	$\frac{-11\phi_r(x)+18\phi_r(x+s)-9\phi_r(x+2s)+2\phi_r(x+3s)}{6s}$	$O(s^3)$	20/3	1/4
Central	$\frac{\phi_r(x+3s)-9\phi_r(x+2s)+45\phi_r(x+s)-45\phi_r(x-s)+9\phi_r(x-2s)-\phi_r(x-3s)}{60s}$	$O(s^6)$	5/3	1/150

Table A.4
Bivariate finite difference formulae for first-order mixed derivatives

Method	Formula	Order of Accuracy ($\boldsymbol{p}$)	$\sum \lvert \boldsymbol{C_i} \rvert$	$\boldsymbol{T}$
Backward-Backward	$\frac{\phi_r(x_1,x_2)-\phi_r(x_1-s,x_2)-\phi_r(x_1,x_2-s)+\phi_r(x_1-s,x_2-s)}{s^2}$	$O(s)$	4	1/2
Forward-Forward	$\frac{\phi_r(x_1+s,x_2+s)-\phi_r(x_1,x_2+s)-\phi_r(x_1+s,x_2)+\phi_r(x_1,x_2)}{s^2}$	$O(s)$	4	1/2
Central-Central	$\frac{\phi_r(x_1+s,x_2+s)-\phi_r(x_1-s,x_2+s)-\phi_r(x_1+s,x_2-s)+\phi_r(x_1-s,x_2-s)}{4s^2}$	$O(s^2)$	1	1/12

Table A.5
Bivariate finite difference formula for second-order mixed derivatives

Method	Formula	Order of Accuracy ($\boldsymbol{p}$)	$\sum \lvert \boldsymbol{C_i} \rvert$	$\boldsymbol{T}$
Backward-Backward (2nd-1st)	$\frac{3\phi_r(x_1,x_2)-4\phi_r(x_1-s,x_2)+\phi_r(x_1-2s,x_2)-3\phi_r(x_1,x_2-s)+4\phi_r(x_1-s,x_2-s)-\phi_r(x_1-2s,x_2-s)}{2s^2}$	$O(s^2)$	16	1/3
Forward-Forward (2nd-1st)	$\frac{-3\phi_r(x_1,x_2)+4\phi_r(x_1+s,x_2)-\phi_r(x_1+2s,x_2)+3\phi_r(x_1,x_2+s)-4\phi_r(x_1+s,x_2+s)+\phi_r(x_1+2s,x_2+s)}{2s^2}$	$O(s^2)$	16	1/3

These tables provide the necessary coefficients (C_i), truncation coefficients (T), and sums of absolute coefficients ($\sum |C_i|$) required for implementing both univariate and bivariate finite difference schemes and for calculating the optimum spacing as presented in Section 2.2.

Appendix B. STL Slicing and Geometric Feature Extraction

The STL slicing algorithm processes triangular mesh data to generate cross-sectional geometry and extract features essential for subsequent machine learning classification. The mathematical foundations of this process are detailed below.

B.1. STL Representation and Plane Intersection

An STL file represents a 3D object as a collection of triangular facets. Each facet is defined by three vertices and a normal vector. Let a triangular facet be represented by its vertices

$$P_1=(x_1,y_1,z_1),P_2=(x_2,y_2,z_2),P_3=(x_3,y_3,z_3) \tag{86}$$

For slicing, a horizontal plane at height

$$z=z_{\text{slice}} \tag{87}$$

is defined. The intersection between this plane and a facet occurs if and only if

$$\min(z_1,z_2,z_3)\le z_{\text{slice}}\le \max(z_1,z_2,z_3) \tag{88}$$

When an intersection exists, the algorithm computes the intersection points. For an edge connecting vertices P_i and P_j that crosses the slice plane, the intersection point P_{int} is calculated via linear interpolation

$$P_{\text{int}}=P_i+t(P_j-P_i) \tag{89}$$

with the interpolation parameter given by

$$t=\frac{z_{\text{slice}}-z_i}{z_j-z_i} \tag{90}$$

This yields the intersection coordinates

$$x_{\text{int}}=x_i+t(x_j-x_i),y_{\text{int}}=y_i+t\left(y_j-y_i\right),z_{\text{int}}=z_{\text{slice}} \tag{91}$$

B.2. Contour Formation

The intersection points from all facets at a given slice height form disconnected line segments. These segments are assembled into closed contours using graph theory. Define a graph

$$G=(V,E) \tag{92}$$

where vertices V correspond to intersection points and edges E represent the line segments. Two intersection points P_a and P_b are considered identical (and merged) if

$$\| P_a - P_b \|_2 < \epsilon \tag{93}$$

with ϵ a small tolerance (typically 10^{-8}). A connectivity matrix C is built such that

$$C_{ij} = \begin{cases} 1, & \text{if vertices } i \text{ and } j \text{ are connected,} \\ 0, & \text{otherwise.} \end{cases} \tag{94}$$

Connected components are then identified (using, for example, depth-first search), yielding a set of closed contours $\{C_1, C_2, \ldots, C_n\}$ for each slice.

B.3. Geometric Feature Extraction

For each closed contour C_k defined by vertices $\{v_1, v_2, \ldots, v_m\}$ where $v_i = (x_i, y_i)$, various geometric features are computed.

B.3.1 Area

The area of the polygon is computed using the shoelace formula

$$A = \frac{1}{2} \left| \sum_{i=1}^{m} (x_i y_{i+1} - x_{i+1} y_i) \right|, \tag{95}$$

with $v_{m+1} = v_1$ to close the contour.

B.3.2 Centroid

The centroid (x_c, y_c) is calculated as

$$x_c = \frac{1}{6A} \sum_{i=1}^{m} (x_i + x_{i+1})(x_i y_{i+1} - x_{i+1} y_i) \tag{96}$$

$$y_c = \frac{1}{6A} \sum_{i=1}^{m} (y_i + y_{i+1})(x_i y_{i+1} - x_{i+1} y_i) \tag{97}$$

B.3.4 Moments of Inertia

The second moments (moments of inertia) are computed by

$$I_x = \frac{1}{12} \sum_{i=1}^{m} \left(y_i^2 + y_i y_{i+1} + y_{i+1}^2 \right)(x_i y_{i+1} - x_{i+1} y_i) \tag{98}$$

$$I_y = \frac{1}{12} \sum_{i=1}^{m} \left(x_i^2 + x_i x_{i+1} + x_{i+1}^2 \right)(x_i y_{i+1} - x_{i+1} y_i) \tag{99}$$

and the product moment is

$$I_{xy} = \frac{1}{24} \sum_{i=1}^{m} (x_i y_{i+1} + 2x_i y_i + 2x_{i+1} y_{i+1} + x_{i+1} y_i)(x_i y_{i+1} - x_{i+1} y_i) \tag{100}$$

B.3.5 Perimeter

The perimeter is the sum of Euclidean distances between consecutive vertices

$$P = \sum_{i=1}^{m} \sqrt{(x_{i+1} - x_i)^2 + (y_{i+1} - y_i)^2} \tag{101}$$

B.3.6 Aspect Ratio

The aspect ratio is defined via the eigenvalues of the covariance matrix of vertex coordinates

$$C_{ov} = \begin{bmatrix} \sigma_{xx} & \sigma_{xy} \\ \sigma_{xy} & \sigma_{yy} \end{bmatrix}, \tag{102}$$

where σ_{xx}, σ_{yy}, and σ_{xy} are normalised second central moments. With eigenvalues λ_1 and λ_2, the aspect ratio is

$$AspectRatio = \sqrt{\frac{\max(\lambda_1, \lambda_2)}{\min(\lambda_1, \lambda_2)}} \tag{103}$$

B.3.6 Curvature

Local curvature κ_i at vertex v_i (using three consecutive vertices) is approximated by

$$\kappa_i = \frac{2\det(v_{i+1} - v_i, v_{i-1} - v_i)}{\| v_{i+1} - v_i\|_2 \cdot \|v_{i-1} - v_i\|_2 \cdot \|v_{i+1} - v_{i-1}\|_2} \tag{104}$$

The mean curvature over the contour is then

$$\kappa_{\text{mean}} = \frac{1}{m}\sum_{i=1}^{m} \kappa_i \tag{105}$$

B.3.7 Relative Position Features

Additional features capture the relative position of the slice to the whole model.

- Height Ratio (H_R): The normalised z-position of the slice,

$$H_R = \frac{z_{\text{slice}} - z_{\min}}{z_{\max} - z_{\min}} \tag{106}$$

- Distance from Centre (D_c): The normalised distance from the contour centroid to the global centre,

$$D_c = \frac{\sqrt{x_c^2 + y_c^2}}{\sqrt{A_{\max}}} \tag{107}$$

where $A_{\max}$ is the maximum contour area in the slice.

These geometric features form the input vector for the machine learning model that classifies each contour into its corresponding component (body, holder, channel, or insert).

Appendix C. Machine Learning Component Classification

After geometric feature extraction, machine learning is employed to classify components within the cutting tool.

C.1. Feature Selection

A chi-square (χ^2) feature selection method is implemented. Given a feature vector $\mathbf{X} = [x_1, x_2, \ldots, x_n]$ and class labels $\mathbf{Y} = [y_1, y_2, \ldots, y_n]$, the chi-square test evaluates the independence between each feature and the labels. For feature x_j, the chi-square statistic is

$$\chi^2 = \sum_{i=1}^{m}\sum_{k=1}^{c} \frac{(O_{ik} - E_{ik})^2}{E_{ik}}, \tag{108}$$

where.

- m is the number of feature value intervals,
- c is the number of classes,
- O_{ik} is the observed frequency in interval i for class k,
- E_{ik} is the expected frequency,

$$E_{ik} = \frac{n_{i\cdot} \cdot n_{\cdot k}}{n}, \tag{109}$$

with $n_{i\cdot}$ and $n_{\cdot k}$ being the marginal totals and n the total number of samples. A feature is selected if its p-value satisfies:

$$E_{ik} = \frac{n_{i\cdot} \cdot n_{\cdot k}}{n}, \tag{110}$$

with α the significance threshold.

C.2. Feature Normalisation

To equalise the contribution of features with different scales, z-score normalisation is applied

$$x_j' = \frac{x_j - \mu_j}{\sigma_j}, \tag{111}$$

Where,

$$\mu_j = \frac{1}{n}\sum_{i=1}^{n} x_{ij}, \sigma_j = \sqrt{\frac{1}{n}\sum_{i=1}^{n}\left(x_{ij}-\mu_j\right)^2} \tag{112}$$

This transformation ensures features have zero mean and unit variance.

C.4. Zone-Based Feature Engineering

To incorporate structural context, zoned likelihood features are computed based on the vertical position within the tool. The tool is divided into three zones: body (1), transition (0), and holder (−1). For a slice at height ratio h_r, the zone is determined by analysing outer diameter distributions. Significant transitions are identified where

$$\left|\frac{D_i - D_{i-1}}{D_{i-1}}\right| > \tau_D \tag{113}$$

with τ_D a diameter transition threshold. A zone confidence vector

$$\mathrm{Z} = [z_1, z_2, \ldots, z_n] \tag{114}$$

is defined as

$$z_i = \begin{cases} z_{\text{high}}, & \text{if zone}_i \in \{-1, 1\} \\ z_{\text{mid}}, & \text{if zone}_i = 0 \end{cases} \tag{115}$$

For each component, zoned likelihoods L_{body}, L_{holder}, and $L_{channel}$ are computed based on size, position, and zone classification. These likelihoods are normalised and incorporated into the feature vector, so

$$L_{body} + L_{holder} + L_{channel} = 1 \tag{116}$$

Support Vector Machine Classification

The classification model employs a Support Vector Machine (SVM) with a Gaussian kernel. Given a normalised feature vector $\mathbf{x}$, the SVM decision function for multi-class classification is

$$f(\mathbf{x}) = \arg\max_{k\in\{1,\ldots,K\}} \sum_{i=1}^{n} \alpha_{i,k}\, y_{i,k}\, K(\mathbf{x}_i, \mathbf{x}) + b_k \tag{117}$$

where.

- K is the number of classes,
- $\alpha_{i,k}$ are the dual coefficients,
- $y_{i,k}$ are binary class indicators,
- b_k is the bias for class k,

The Gaussian kernel is defined as

$$K(\mathbf{x}_i, \mathbf{x}) = \exp\left(-\gamma\|\mathbf{x}_i - \mathbf{x}\|^2\right) \tag{118}$$

with γ controlling the influence radius. The SVM is trained via sequential minimal optimisation to solve the associated quadratic programming problem.

C.5. Material Property Calculation

Once the components within each slice are classified, their material properties are combined to determine the effective properties of the entire slice.

C.5.1. Material Assignment

For each classified component, material properties are assigned based on its type. Let Ω_k denote the set of contours in a slice classified as component type $k \in \{\text{body}, \text{holder}, \text{channel}, \text{insert}\}$. Each component type has associated material properties $\Psi_k = \{\psi_k^1, \psi_k^2, \ldots, \psi_k^m\}$.

C.5.2. General Mixing Law

For a slice containing n contours with areas $\{A_1, A_2, \ldots, A_n\}$ and material properties $\left\{\psi_1^j, \psi_2^j, \ldots, \psi_n^j\right\}$ for property j, the effective property is calculated as:

$$\psi^j_{\text{eff}} = \frac{\sum_{i=1}^{n} w_i \, \psi^j_i \, A_i}{\sum_{i=1}^{n} w_i \, A_i} \tag{119}$$

where w_i is a weighting factor. For extensive properties (e.g., mass), $w_i = 1$; for others, w_i may vary. More generally, one can express the mixing law as

$$\psi^j_{\text{eff}} = f_j\left(\left\{\left(\psi^j_i, A_i, g_i\right)\right\}_{i=1}^{n}\right) \tag{120}$$

with g_i representing geometric arrangement.

C.5.3 Effective Mechanical Properties

For properties relevant to beam theory, effective values are computed using functions such as

$$\psi^j_{\text{eff}} = \begin{cases} f_{\text{arithmetic}}\left(\left\{\psi^j_i, A_i\right\}\right), & \text{(rule of mixtures)} \\ f_{\text{harmonic}}\left(\left\{\psi^j_i, A_i\right\}\right), & \text{(inverse rule of mixtures)} \\ f_{\text{geometric}}\left(\left\{\psi^j_i, A_i, I_i\right\}\right), & \text{(moment-dependent)} \end{cases} \tag{121}$$

The effective cross-sectional properties are computed as

$$A_{\text{eff}} = \sum_{i=1}^{n} A_i, \tag{122}$$

$$I_{x,\text{eff}} = \sum_{i=1}^{n} I_{x,i} + \sum_{i=1}^{n} A_i \left(y_{c,i} - y_c\right)^2, \tag{123}$$

$$I_{y,\text{eff}} = \sum_{i=1}^{n} I_{y,i} + \sum_{i=1}^{n} A_i \left(x_{c,i} - x_c\right)^2, \tag{124}$$

$$I_{xy,\text{eff}} = \sum_{i=1}^{n} I_{xy,i} + \sum_{i=1}^{n} A_i \left(x_{c,i} - x_c\right)\left(y_{c,i} - y_c\right) \tag{125}$$

where (x_c, y_c) is the overall centroid.

C.5.4 Handling hole Regions

For regions classified as channels (holes), which affect geometry but not material properties, the effective property is adjusted as:

$$\psi^j_{\text{eff,adjusted}} = \frac{\sum_{i \notin \Omega_{hole}} w_i \, \psi^j_i \, A_i}{\sum_{i=1}^{n} w_i \, A_i - A_{hole}} \tag{126}$$

where A_{hole} is the total area of hole regions.

Data availability

Data will be made available on request.

References

[1] T. Schmitz, E. Betters, E. Budak, E. Yüksel, S. Park, Y. Altintas, Review and status of tool tip frequency response function prediction using receptance coupling, Precis. Eng. 79 (Jan. 2023) 60–77, https://doi.org/10.1016/J.PRECISIONENG.2022.09.008.

[2] D. De Klerk, D.J. Rixen, S.N. Voormeeren, in: General Framework for Dynamic Substructuring: History, Review and Classification of Techniques, 46, May 2012, pp. 1169–1181, https://doi.org/10.2514/1.33274, doi: 10.2514/1.33274 5.

[3] T.L. Schmitz, R.R. Donalson, Predicting high-speed machining dynamics by substructure analysis, CIRP Annals 49 (1) (Jan. 2000) 303–308, https://doi.org/10.1016/S0007-8506(07)62951-5.

[4] A. Ertürk, H.N. Özgüven, E. Budak, Analytical modeling of spindle–tool dynamics on machine tools using Timoshenko beam model and receptance coupling for the prediction of tool point FRF, Int. J. Mach. Tool Manufact. 46 (15) (Dec. 2006) 1901–1912, https://doi.org/10.1016/J.IJMACHTOOLS.2006.01.032.

[5] E.B. Kivanc, E. Budak, Structural modeling of end mills for form error and stability analysis, Int. J. Mach. Tool Manufact. 44 (11) (Sep. 2004) 1151–1161, https://doi.org/10.1016/J.IJMACHTOOLS.2004.04.002.

[6] O. Özşahin, Y. Altintas, Prediction of frequency response function (FRF) of asymmetric tools from the analytical coupling of spindle and beam models of holder and tool, Int. J. Mach. Tool Manufact. 92 (May 2015) 31–40, https://doi.org/10.1016/J.IJMACHTOOLS.2015.03.001.

[7] I. Mancisidor, A. Urkiola, R. Barcena, J. Munoa, Z. Dombovari, M. Zatarain, Receptance coupling for tool point dynamic prediction by fixed boundaries approach, Int. J. Mach. Tool Manufact. 78 (Mar. 2014) 18–29, https://doi.org/10.1016/J.IJMACHTOOLS.2013.12.002.

[8] L.T. Tunc, Prediction of tool tip dynamics for generalized milling cutters using the 3D model of the tool body, Int. J. Adv. Manuf. Technol. 95 (5–8) (Mar. 2018) 1891–1909, https://doi.org/10.1007/S00170-017-1286-X/METRICS.

[9] S.S. Park, S. Amani, D.Y. Lee, J. Lee, E. Nam, Machine learning based substructure coupling of machine tool dynamics and chatter stability, CIRP Annals 73 (1) (Jan. 2024) 297–300, https://doi.org/10.1016/J.CIRP.2024.04.088.

[10] J. Liao, J. Zhang, P. Feng, D. Yu, Z. Wu, Identification of contact stiffness of shrink-fit tool-holder joint based on fractal theory, Int. J. Adv. Manuf. Technol. 90 (5–8) (May 2017) 2173–2184, https://doi.org/10.1007/S00170-016-9506-3/METRICS.

[11] H. Miao, et al., A fully analytical nonlinear dynamic model of spindle-holder-tool system considering contact characteristics of joint interfaces, Mech. Syst. Signal Process. 202 (Nov. 2023) 110693, https://doi.org/10.1016/J.YMSSP.2023.110693.

[12] T. Schmitz, A. Honeycutt, M. Gomez, M. Stokes, E. Betters, Multi-point coupling for tool point receptance prediction, J. Manuf. Process. 43 (Jul. 2019) 2–11, https://doi.org/10.1016/J.JMAPRO.2019.03.043.

[13] S.S. Park, Y. Altintas, M. Movahhedy, Receptance coupling for end mills, Int. J. Mach. Tool Manufact. 43 (9) (Jul. 2003) 889–896, https://doi.org/10.1016/S0890-6955(03)00088-9.
[14] T.L. Schmitz, G.S. Duncan, Three-component receptance coupling substructure analysis for tool point dynamics prediction, J. Manuf. Sci. Eng. 127 (4) (Nov. 2005) 781–790, https://doi.org/10.1115/1.2039102.
[15] P. Albertelli, M. Goletti, M. Monno, A new receptance coupling substructure analysis methodology to improve chatter free cutting conditions prediction, Int. J. Mach. Tool Manufact. 72 (Sep. 2013) 16–24, https://doi.org/10.1016/J.IJMACHTOOLS.2013.05.003.
[16] Y. Ji, Q. Bi, S. Zhang, Y. Wang, A new receptance coupling substructure analysis methodology to predict tool tip dynamics, Int. J. Mach. Tool Manufact. 126 (Mar. 2018) 18–26, https://doi.org/10.1016/J.IJMACHTOOLS.2017.12.002.
[17] K. Kiran, H. Satyanarayana, T. Schmitz, Compensation of frequency response function measurements by inverse RCSA, Int. J. Mach. Tool Manufact. 121 (Oct. 2017) 96–100, https://doi.org/10.1016/J.IJMACHTOOLS.2017.04.004.
[18] H.S. Kim, T.L. Schmitz, Bivariate uncertainty analysis for impact testing, Meas. Sci. Technol. 18 (11) (Oct. 2007) 3565, https://doi.org/10.1088/0957-0233/18/11/041.
[19] M. Wan, Y.Y. Ren, W.H. Zhang, Y. Yang, Investigation of a cutting state-independent method for identifying in-process frequency response functions of the micro milling system, Mech. Syst. Signal Process. 213 (May 2024) 111353, https://doi.org/10.1016/J.YMSSP.2024.111353.
[20] Y. Ji, H. Dong, L. Yu, F. Ren, Q. Bi, Y. Wang, Determining rotating tool-tip FRFs by measuring holder-point FRFs based on a robust frequency-based substructure method, Mech. Syst. Signal Process. 164 (Feb. 2022) 108228, https://doi.org/10.1016/J.YMSSP.2021.108228.
[21] Y. Ji, Y. Yu, Q. Bi, H. Zhao, Calibration rod selection strategy in RCSA-based method for reliable calculation of milling tool-tip FRFs in rotating conditions, Int. J. Mach. Tool Manufact. 187 (Apr. 2023) 104016, https://doi.org/10.1016/J.IJMACHTOOLS.2023.104016.
[22] S.S. Sattinger, A Method for Experimentally Determining Rotational Mobilities, Massachusetts Institute of Technology, Cambridge, Massachusetts, 1978. M.S. Thesis.
[23] David Eberly, Derivative Approximation by Finite Differences, Redmond WA, Feb. 2020 [Online]. Available: https://www.geometrictools.com/Documentation/FiniteDifferences.pdf. (Accessed 20 June 2024).
[24] D.J. Ewins, Modal Testing: Theory, Practice and Application, second ed., Research Studies Press, Philadelphia, PA, 2000.
[25] O. Özşahin, E. Budak, H.N. Özgüven, Identification of bearing dynamics under operational conditions for chatter stability prediction in high speed machining operations, Precis. Eng. 42 (Oct. 2015) 53–65, https://doi.org/10.1016/J.PRECISIONENG.2015.03.010.
[26] T.J. Gibbons, E. Öztürk, N.D. Sims, Rotational degree-of-freedom synthesis: an optimised finite difference method for non-exact data, J. Sound Vib. 412 (Jan. 2018) 207–221, https://doi.org/10.1016/J.JSV.2017.09.031.
[27] Y. Ji, Y. Chen, S. Zhang, Q. Bi, Y. Wang, Multi-point substructure coupling method to compensate multi-accelerometer masses in measuring rotation-related frequency response functions, Journal of Manufacturing Science and Engineering, Transactions of the ASME 144 (1) (Jan. 2022), https://doi.org/10.1115/1.4051534/1111568.
[28] M.M. Hafez, L.C. Wellford, C.L. Merkle, E.M. Murman, Numerical Computation of Transonic Flows by Finite-Element and Finite-Difference Methods, 1978.
[29] J.R. Hutchinson, Shear coefficients for Timoshenko beam theory, J. Appl. Mech. 68 (1) (Jan. 2001) 87–92, https://doi.org/10.1115/1.1349417.
[30] S.S. Park, S. Amani, D.Y. Lee, J. Lee, E. Nam, Machine learning based substructure coupling of machine tool dynamics and chatter stability, CIRP Annals (May 2024), https://doi.org/10.1016/J.CIRP.2024.04.088.
[31] P. Lechner, L. Scandola, D. Maier, C. Hartmann, Y. Rizaiev, M. Lieb, A physically-informed machine learning model for freeform bending, J. Intell. Manuf. (Jul. 2024) 1–13, https://doi.org/10.1007/S10845-024-02452-W/FIGURES/19.
[32] X. Lazkano, P. Aristimuño, P. Arrazola, Improvement of material databases for cutting force prediction in finishing conditions of A-356 aluminium alloy, Proced. CIRP 101 (Jan. 2021) 122–125, https://doi.org/10.1016/J.PROCIR.2020.09.192.
[33] X. Zheng, et al., Exploring the effectiveness of using internal CNC system signals for chatter detection in milling process, Mech. Syst. Signal Process. 185 (Feb. 2023) 109812, https://doi.org/10.1016/J.YMSSP.2022.109812.
[34] S.S. Rao, Mechanical Vibrations, fifth ed., Prentice Hall, Upper Saddle River, NJ, 2011.
[35] M. Namazi, Y. Altintas, T. Abe, N. Rajapakse, Modeling and identification of tool holder–spindle interface dynamics, Int. J. Mach. Tool Manufact. 47 (9) (Jul. 2007) 1333–1341, https://doi.org/10.1016/J.IJMACHTOOLS.2006.08.003.
[36] T.L. Schmitz, K.S. Smith, Machining Dynamics, 2019, https://doi.org/10.1007/978-3-319-93707-6. Machining Dynamics.